

# A CATALOG OF BULGE+DISK DECOMPOSITIONS AND UPDATED PHOTOMETRY FOR 1.12 MILLION GALAXIES IN THE SLOAN DIGITAL SKY SURVEY

LUC SIMARD<sup>1,2</sup>, J. TREVOR MENDEL<sup>2</sup>, DAVID R. PATTON<sup>3</sup>, SARA L. ELLISON<sup>2</sup>, ALAN W. MCCONNACHIE<sup>1</sup>

*Accepted on June 3, 2011 for Publication in Astrophysical Journal Supplements*

## ABSTRACT

We perform two-dimensional, Point-Spread-Function-convolved, bulge+disk decompositions in the  $g$  and  $r$  bandpasses on a sample of 1,123,718 galaxies from the Legacy area of the Sloan Digital Sky Survey Data Release Seven. Four different decomposition procedures are investigated which make improvements to sky background determinations and object deblending over the standard SDSS procedures that lead to more robust structural parameters and integrated galaxy magnitudes and colors, especially in crowded environments. We use a set of science-based quality assurance metrics namely the disk luminosity-size relation, the galaxy color-magnitude diagram and the galaxy central (fiber) colors to show the robustness of our structural parameters. The best procedure utilizes simultaneous, two-bandpass decompositions. Bulge and disk photometric errors remain below 0.1 mag down to bulge and disk magnitudes of  $g \simeq 19$  and  $r \simeq 18.5$ . We also use and compare three different galaxy fitting models: a pure Sérsic model, a  $n_b = 4$  bulge + disk model and a Sérsic (free  $n_b$ ) bulge + disk model. The most appropriate model for a given galaxy is determined by the  $F$ -test probability. All three catalogs of measured structural parameters, rest-frame magnitudes and colors are publicly released here. These catalogs should provide an extensive comparison set for a wide range of observational and theoretical studies of galaxies.

*Subject headings:* galaxies : fundamental parameters, galaxies : evolution

## 1. INTRODUCTION

The properties of disks and spheroids in the local Universe are the direct outcomes of the hierarchical assembly of galaxies over cosmological time. It is well known that the structural parameters of these important galaxy sub-components obey scaling relations between size, luminosity and internal velocity (e.g., Courteau et al. 2007). The amount of stellar mass found in disks and bulges places strong constraints on the galaxy merger tree from  $\Lambda$ CDM N-body simulations (Hopkins et al. 2010) and the secular formation of bulges (e.g., Kormendy 1979; Athanassoula 2003). Some properties such as disk size can be traced to properties of host dark matter haloes such as specific angular momentum (Fall & Efstathiou 1980; Mo, Mao & White 1998), and more information is needed for a truly large sample of galaxies to improve the recipes used in semi-analytical approaches to the treatment of the so-called “sub-grid” physics (Governato et al. 2004; Robertson et al. 2004; Dutton & van den Bosch 2009).

Thanks to the availability of large datasets and powerful computing clusters, it is now possible to analyze large samples of galaxies in a fully quantitative way. Quantitative measurements of galaxy properties have made significant progress over the last few years (Peng et al. 2002; Simard et al. 2002; de Souza et al. 2004; Lotz et al. 2004; Conselice 2006; Pignatelli et al. 2006) and now provide an important framework for

comparisons between observation and theory. A number of previous works have looked at the morphologies of SDSS galaxies using a wide range of subsamples and techniques (Shen et al. 2003; Blanton et al. 2005a; Kelly & McKay 2005; Benson et al. 2007; Fukugita et al. 2007; Lintott et al. 2008; La Barbera et al. 2010; Wijesinghe et al. 2010). This paper presents the largest catalog of bulge+disk structural parameters measured to date of galaxies in the Sloan Digital Sky Survey Data Release Seven (SDSS DR7, Abazajian et al. 2009). This catalog has already been used to study visual versus quantitative morphologies (Cheng et al. 2010), galaxy pairs (Ellison et al. 2008, 2010; Patton et al. 2011), disk scaling relations at low and high redshift (Dutton et al. 2011a,b), the disk size function (Kanwar et al. 2008, and Simard 2011, in preparation), the evolution of cluster galaxies with redshift (Simard et al. 2009), compact groups of galaxies (Mendel et al. 2011), and the disk and bulge stellar mass functions (Thanjavur & Simard 2011). The paper is organized as follows. The data and the bulge+disk decompositions are described in Sections 2 and 3. The catalog, science-based quality assessment metrics and a comparison between different fitting models are presented in Section 4. The cosmology adopted throughout this paper is  $(H_0, \Omega_m, \Omega_\Lambda) = (70 \text{ km s}^{-1} \text{ Mpc}^{-1}, 0.3, 0.7)$ .

## 2. DATA

The data come from the Legacy area of the SDSS. We selected a photometric sample from the **PhotoPrimary** table. The two main galaxy selection criteria were Petrosian magnitude (corrected for Galactic extinction) and morphological classification. We first selected objects with  $14 \leq m_{\text{petro},r,\text{corr}} \leq 18$ , where  $m_{\text{petro},r,\text{corr}}$  is the  $r$ -band Petrosian magnitude corrected for Galactic extinction according to the extinction values given in the

<sup>1</sup> National Research Council of Canada, Herzberg Institute of Astrophysics, 5071 West Saanich Road, Victoria, British Columbia, Canada

<sup>2</sup> Department of Physics and Astronomy, University of Victoria, Victoria, British Columbia, V8P 1A1, Canada

<sup>3</sup> Department of Physics and Astronomy, Trent University, 1600 West Bank Drive, Peterborough, Ontario, K9J 7B8, Canada

SDSS database. We also selected extended objects with morphological type `Type=3`. In addition to these two criteria, we also required that the sum of the flags `DEBLENDED_AS_PSF` and `SATURATED` be zero to eliminate objects that were found to be unresolved children of their parents as well as saturated objects. The full query reads:

```
select objid from dr7.PhotoPrimary where
flags & (dbo.fPhotoFlags('SATURATED') +
dbo.fPhotoFlags('DEBLENDED_AS_PSF'))= 0 and
(petroMag_r-extinction_r) between 14.0 and 18.0
and Type=3.
```

This query returned 2,195,875 objects from the SEGUE and Legacy areas. In order to select only objects from the Legacy area, we used the DR7 sky coverage table `allrunsdr7db.par`<sup>4</sup> to obtain the list of run/rerun combinations in this area, and we then filtered the output of the query using the list. The total number of objects in our Legacy-area photometric sample is 1,123,718.

Given the importance of the links between the morphological and spectroscopic properties of galaxies, we also defined a spectroscopic galaxy sample by selecting objects from our photometric sample with  $m_{\text{petro},r,\text{corr}} \leq 17.77$  and the spectrum of a galaxy as defined by the keyword `SpecClass` in the `SpecPhoto` database table. Specifically, we selected objects with `SpecPhoto.SpecClass=2`. These spectroscopic selection criteria yielded 674,701 galaxies. The faint limit is the completeness limit of the SDSS Main Galaxy spectroscopic sample (Strauss et al. 2002). As discussed in Strauss et al. (2002), the nominal surface brightness limit of the SDSS spectroscopic sample is  $r$ -band  $\mu_{50,r} = 24.5$  mag arcsec<sup>-2</sup>. However, objects in the range  $23.0$  mag arcsec<sup>-2</sup>  $\leq \mu_{50,r} \leq 24.5$  mag arcsec<sup>-2</sup> were targeted only when the local and global sky values were within  $0.05$  mag arcsec<sup>-2</sup> of one another. We therefore set the faint surface brightness limit of our spectroscopic sample to  $\mu_{50,r} = 23.0$  mag arcsec<sup>-2</sup> to retain a complete sample. This limit further cuts the number of galaxies down to 671,425. The number of objects excluded by this cut is small as expected from Figure 1. Following Shen et al. (2003), we then excluded a small number of galaxies with redshift  $z < 0.005$  whose distances may be severely contaminated by their peculiar velocities. The final total number of objects satisfying our spectroscopic selection criteria was 670,131.

$g$ - and  $r$ -band images of all galaxies in our photometric sample were analyzed as described in Section 3. The redshift distribution for the spectroscopic sample is shown in Figure 2. The bulk of the sample is at  $z \sim 0.1$ . The peaks in this distribution are due to real large-scale structures within the SDSS survey volume.

### 3. ANALYSIS

#### 3.1. Preprocessing of SDSS Images

Information for each galaxy to be analyzed was fetched directly from the SDSS catalog server using a remote data mining pipeline based on the Python programming language and the `wget` protocol. The fields `objID`, `ra`, `dec`, `run`, `rerun`, `camcol`, `field`, `obj`, `petroMag_r`, `z`, and `extinction_r` were extracted from

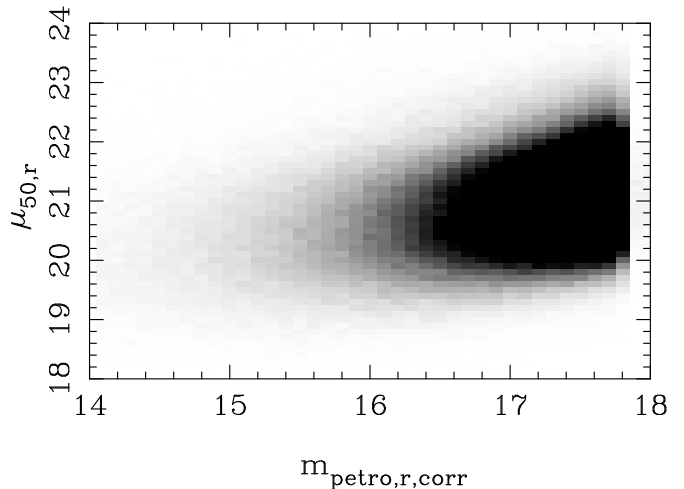


**Figure 1.** Apparent  $r$ -band Petrosian magnitude and surface brightness distribution of galaxies in our photometric sample. Corrected for Galactic extinction using SDSS values.

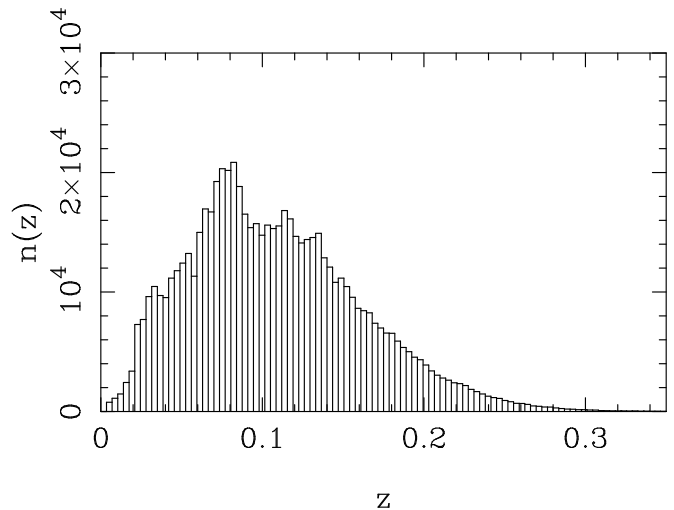


**Figure 2.** Redshift distribution of galaxies in our spectroscopic sample ( $14 \leq m_{\text{petro},r,\text{corr}} \leq 17.77$ ,  $\mu_{50,r} \leq 23$  mag arcsec<sup>-2</sup>, `SpecPhoto.SpecClass=2`).

the `PhotoPrimary` table. The atlas (prefix “fpAtlas”), corrected (prefix “fpC”) and point-spread-function (prefix “psField”) images were then retrieved directly from the SDSS Data Archive Server (DAS). The locations of these images for a given galaxy were given by `run`, `rerun` and `camcol`. Galaxy positions (`rowc` and `colc`) on the corrected images were also extracted from `PhotoPrimary`. The SDSS corrected images are survey images that have been bias subtracted, flat-fielded and purged of bright stars.

Our bulge+disk decomposition procedure requires input thumbnail images for each object. These thumbnails were prepared from SDSS images using the following pre-processing steps: (1) extraction of the atlas and point-spread-function images, (2) creation of the science thumbnail images, and (3) creation of the mask thumbnail image. We used the SDSS software utilities `readAtlasImages`<sup>5</sup> and `read_PSF`<sup>6</sup> for the atlas and PSF

<sup>4</sup> <http://www.sdss.org/dr7/coverage/allrunsdr7db.par>

<sup>5</sup> [http://www.sdss.org/dr7/products/images/read\\_atlas.html](http://www.sdss.org/dr7/products/images/read_atlas.html)

<sup>6</sup> [http://www.sdss.org/dr7/products/images/read\\_psf.html](http://www.sdss.org/dr7/products/images/read_psf.html)

images respectively. `readAtlasImages` requires a bandpass and object ID as inputs while `readPSF` can output a SDSS-provided PSF at any object position (given by `rowc`, `colc`) in a given bandpass.

### 3.2. Defining Objects on SDSS images

There is no unique procedure for deblending objects and defining their object-sky boundaries on astronomical images. Two different approaches can be adopted to tackle this problem, and these two approaches are exemplified by the SDSS *PHOTO* pipeline and the SExtractor software (Bertin & Arnouts 1996). Both approaches are shown in Figure 3. In the case of SDSS deblending (Section 3.2.1), the pipeline tries to isolate the flux in a given object to create a new image of what this object would look like if only this flux was shown. The object area of interest is then determined from this new deblended image. It is important to note that this object area may extend to areas that used to be occupied by neighboring galaxies, and may affect the photometry if some flux from the neighboring galaxies that were removed is left behind. SExtractor deblending (Section 3.2.2) does not attempt to create a new image showing the deblended object. It uses a multi-threshold method to look at the flux tree of the object in its original image. As it moves up the tree going from one isophotal level to the next, it looks at the flux in each branch. If the flux in a branch is above a set minimum fraction of the total flux in the tree, then this branch is deemed to be a separate object altogether. Once all the objects have been identified, SExtractor then produces a segmentation image that assigns pixels to the different objects. In the case of a galaxy with a close neighbor, the net result is a “ridge” of segmentation values at the saddle point between the two adjacent objects. The segmentation of an object never extends over the area occupied by its neighbors (see upper left-hand panel of Figure 3). It is clear from Figure 3 that each object segmentation area misses a significant fraction of the flux in the object because it spills over into the segmentation area of its neighbor. The SExtractor magnitudes measured from these areas would therefore systematically underestimate the brightnesses of the two objects. However, if we also fit some surface brightness model (e.g., bulge+disk) to the flux inside a given object segmentation area and then integrate the flux in this model out to large radii, then the missing flux is recovered. As we will show later, such combination of SExtractor deblending *and* model photometry can produce more reliable magnitudes and colors in crowded environments.

#### 3.2.1. SDSS Deblending

The atlas images provide object fluxes in pixels deemed to belong to the object by the SDSS deblending algorithm (Lupton et al. 2001), and they have zero object flux everywhere else. The SDSS pipeline adds a constant “softbias” level of 1000 counts to all pixels in the atlas and PSF images. This softbias level was subtracted from the images, so the atlas image sky pixels therefore have a value of zero. However, these atlas images cannot be used as is for our morphological analysis. The isophotal cut chosen to define an object is too high, and the wings of galaxy profiles where useful information can still be

found have been truncated from these images as a result of this choice. Our science thumbnail images were therefore produced by extending the object pixel area in the atlas images using pixels from the corrected image of the field in which the object resides. We ran SExtractor on the corrected image to identify sky pixels. Pixels from the corrected image were added to the science thumbnail only if they were identified as sky pixels.

The mask image is a critical element of the analysis as it specifies the object pixel brightness distribution that will be “seen” by the fitting algorithm. Mask pixels could take on three different values: 1 (object), 0 (sky) and -2 (excluded from fit). Initially, our main consideration was to remain consistent with the object deblending performed by the SDSS pipeline. We did not perform our own object deblending at first. We used the atlas image itself as a starting point for the creation of the mask image. For pixels in the mask image overlapping with the atlas image, we assigned them a value of 1 when the atlas image pixel value was greater than 1000 and a value of -2 otherwise. We then used the SExtractor segmentation image of the corrected image to complete the mask. Pixels in the final mask were assigned a value of 1 if atlas mask pixel value was 1 and a value of 0 if atlas mask was -2 and SExtractor mask value was 0. The net result was a mask with the same dimensions as the atlas image but with more sky pixels than the original atlas images that preserves the object deblending of the SDSS pipeline.

#### 3.2.2. SExtractor Deblending

The procedure for preparing GIM2D postage stamp images using SExtractor rather than SDSS deblending is considerably simpler. It starts directly from the SDSS corrected image frame on which the object is located. SExtractor was run on this corrected frame to measure the parameters `X_IMAGE`, `Y_IMAGE`, `BACKGROUND`, and `ISOAREA_IMAGE` using a value of 0.00005 for the SExtractor deblending contrast parameter `DEBLEND_MINCONT` and a 1- $\sigma$  isophote for the analysis area. The area extracted around each object for the GIM2D postage stamp images was set to five times the area given by `ISOAREA_IMAGE`. The GIM2D decompositions were performed over all pixels flagged as object *or* background in the SExtractor segmentation image. Objects in the segmentation images of the SDSS corrected frames are sharply delineated by the location of the isophote corresponding to the detection threshold because SExtractor considers all pixels below this threshold to be background pixels. However, precious information on the outer parts of the galaxy profile may be contained in the pixels below that threshold, and fits should therefore not be restricted only to object pixels to avoid throwing that information away (This is an analogous problem to the sharp isophotal limit in SDSS atlas images). Pixels belonging to objects in the neighborhood of the primary object being fit are masked out of the fitting area using the SExtractor segmentation image. As noted earlier, the flux from the primary object that would have been in those masked areas in the absence of neighbors is nonetheless properly included in the magnitude measurements because GIM2D magnitudes were obtained by integrating the best-fit models over all pixels.

### 3.3. Sky Background Level Determination

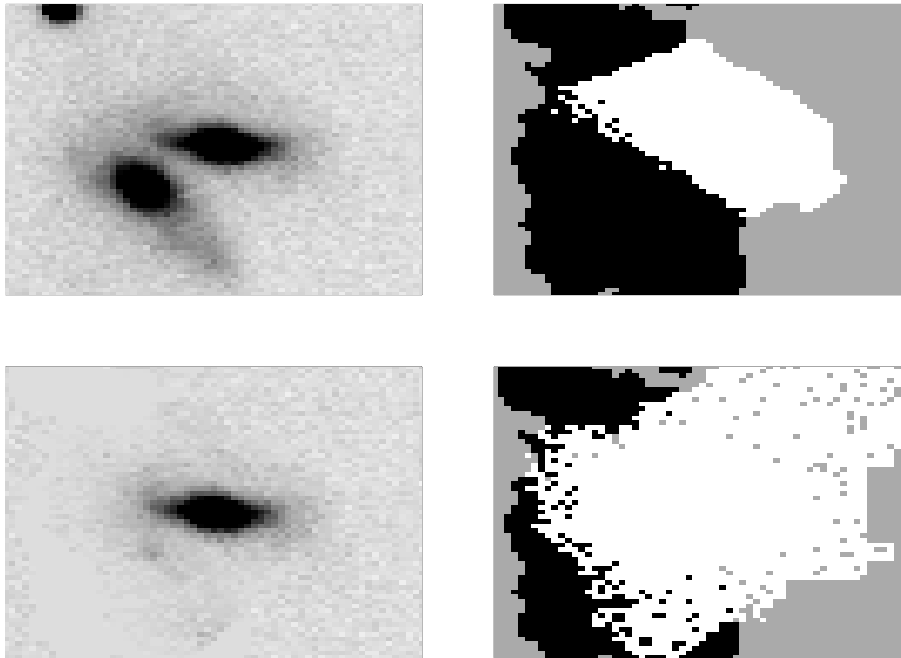


**Figure 3.** The difference between SDSS and SExtractor debblending for object SDSS ObjID = 587729781199864370. This is the central galaxy in the image, and it has a close companion to the lower left. *Top left:* Object image from the SDSS corrected frame. *Top right:* Segmentation pixel mask produced by SExtractor as described in Section 3.2.2. The white region is the area defined as the object by the SExtractor debblending. *Bottom left:* Object image given by the SDSS debbler. *Bottom right:* Segmentation pixel mask constructed from the SDSS debblending as described in Section 3.2.1. The white region is the area defined as the object by the SDSS atlas image. Note how it now extends over the area where the close companion used to be.

Systematic errors in the sky background level determination dominate the errors on the measured structural parameters. An erroneous sky level can also mislead the bulge+disk decomposition algorithm into introducing unphysical bulge or disk components. For example, a very large disk component would result from underestimating the sky level because the positive sky offset would look like such a component to the algorithm. It is therefore critical to measure the best sky possible.

We initially adopted the SDSS sky background levels for our bulge+disk decompositions for the sake of consistency. We used the sky levels given by the keyword SKY in the headers of the corrected images. The sky level for a given corrected frame was subtracted from all the GIM2D science postage stamp images of the objects extracted from this frame. The sky level was then fixed to zero for the bulge+disk decompositions. As discussed later, this procedure did not produce sky background levels that were good enough for our decompositions.

We then used sky background levels and standard deviations determined by GIM2D. GIM2D first uses all the pixels in the science thumbnail image flagged as background pixels (flag value of zero) in the SExtractor segmentation image. GIM2D further prunes this sample of background pixels by excluding any background pixel that is closer than  $4''.0$  from *any* (primary or neighboring) object pixels. This buffer zone ensures that the flux from all SExtracted objects in the image below all the  $1.0\text{-}\sigma_{bkg}$  isophotes does not significantly bias the mean background level upwards and artificially inflate  $\sigma_{bkg}$ . A minimum of 20,000 sky pixels was imposed on the area of the sky region. In cases where the number of sky pixels in the input science thumbnail image was insufficient, the original SDSS corrected image was searched for the

20,000 sky pixels nearest to the object. Background parameters were re-calculated with GIM2D before fitting, and the residual background levels were then frozen to their recalculated values for the bulge+disk fits.

#### 3.4. Two-Dimensional Bulge+Disk Decompositions

Galaxy structural parameters were measured from bulge+disk decompositions performed using version 3.2 of the GIM2D software package (Simard et al. 2002). We used the sum of a pure exponential disk and a de Vaucouleurs bulge (Sérsic index  $n_b = 4$ ) as our galaxy image model. The free fitting parameters of this model were the total flux  $F$  in data units (DU), the bulge fraction  $B/T$  ( $\equiv 0$  for pure disk systems), the bulge semi-major axis effective radius  $r_e$ , the bulge ellipticity  $e$  ( $e \equiv 1 - b/a$ ,  $b \equiv$  semi-minor axis,  $a \equiv$  semi-major axis), the bulge position angle of the major axis  $\phi_b$  on the image (clockwise, y-axis  $\equiv 0$ ), the semi-major axis exponential scale length  $r_d$  (also denoted  $h$  in the literature), the disk inclination  $i$  (face-on  $\equiv 0$ ), the disk position angle  $\phi_d$  on the image, and the  $dx$  and  $dy$  offsets of the model center with respect to the SDSS object position on the sky. The background residual level  $db$  and the bulge Sérsic index  $n_b$  were held fixed for the fits. The position angles  $\phi_b$  and  $\phi_d$  were not forced to be equal for two reasons: (1) a large difference between these position angles is often a signature of strongly barred galaxies, and (2) some observed galaxies do have *bona fide* bulges that are not quite aligned with the disk position angle. In addition to bulge+disk structural parameters, GIM2D computes a variety of asymmetry indices that can be used to quantify galaxy substructure. The impact of substructures on GIM2D measurements has been extensively simulated and discussed in Simard et al. (2002). We *specifically* chose to use a

bulge+disk model rather than a more complicated combination (e.g., bulge+disk+bar(+others)) for the sake of keeping our SDSS measurements consistent with what is achievable with galaxy structural measurements at high-redshift. It is already a challenge to perform reliable bulge+disk decompositions of high redshift galaxy images even with the spatial resolution of the Hubble Space Telescope, and it is not currently possible to use structural models with more components without compromising convergence and avoiding parameter degeneracies.

Fits in the  $g$ - and  $r$ - bands were done using the two-bandpass separate and simultaneous fitting procedures described in Simard et al. (2002). For the separate, two-bandpass fits, the  $g$ - and  $r$ -band images were fitted independently. For the simultaneous, two-bandpass fits, the images were fitted by forcing the bulge radius, ellipticity and position angle and disk scale length, inclination and position angle to take on the same values in both bandpasses. The main advantage of the simultaneous fits is to minimize the errors on the measured structural parameters because all of the data is used at once. Their main disadvantage is that they are blind to color gradients, and significant color gradients would make this approach invalid because sizes would be significantly different in different bandpasses. To test the validity of the application of simultaneous fitting to the SDSS data, we plotted the ratio of the  $g$ -band and  $r$ -band disk scale lengths from separate fits as a function of disk magnitude (Figure 4). The two disk scale lengths are within a few percent of one another and in agreement with a recent cosmologically based disk formation model (Dutton et al. 2011a). As also shown in Figure 4, the bulge effective radii measured separately in the two bandpasses agree to 2%. We therefore deem the simultaneous fitting approach to be valid. There is one important difference between the simultaneous fitting procedure of Simard et al. (2002) and the one used here. Simard et al. (2002) used the same  $dx$  and  $dy$  offsets in both bands because their images had been registered to the same pixel grid in both bands. This is not the case with the SDSS images, and using the same set of offsets produced “positive-negative” residuals in the cores of many galaxies. We therefore let  $dx$  and  $dy$  be different in  $g$  and  $r$ , i.e., we let  $(dx)_g$ ,  $(dy)_r$ ,  $(dx)_r$  and  $(dy)_g$  be free parameters in the simultaneous fits. The simultaneous fits therefore used a total number of fourteen free parameters ( $F_g$ ,  $F_r$ ,  $(B/T)_g$ ,  $(B/T)_r$ ,  $r_e$ ,  $e$ ,  $\phi_b$ ,  $r_d$ ,  $i$ ,  $\phi_d$ ,  $(dx)_g$ ,  $(dx)_r$ ,  $(dy)_g$  and  $(dy)_r$ ).

Four sets of GIM2D fits were performed on the spectroscopic sample defined in Section 2 with different combinations of object deblending, sky level determinations and fitting procedures: (1) Separate fitting + SDSS object deblending + SDSS sky level (“SEP+SDSSDEBL+SDSSBKG”), (2) Separate fitting + SDSS deblending + GIM2D sky level (“SEP+SDSSDEBL+GM2DSKY”), (3) Simultaneous fitting + SDSS deblending + GIM2D sky level (“SIM+SDSSDEBL+GM2DSKY”), and (4) Simultaneous fitting + SExtractor deblending + GIM2D sky level (“SIM+SEXTDEBL+GM2DSKY”). This last set of fits was adopted as our preferred set on the basis of quality assessment tests described in Section 4.1, and the procedure was then run on our full photometric sample of 1.12 million galaxies. Out of all the galaxies in this sample, required files could not be obtained from the SDSS im-

age server for 58 galaxies, and GIM2D convergence was not achieved for 7361 objects (failure rate of 0.66%). Visual inspection of these failures traced most of them back to artefacts (e.g., image defects, bright star spikes, bits of a “shredded” galaxy) in the SDSS catalog. Figure 5 shows a detailed example of a bulge+disk decomposition of a single galaxy, and the summary decompositions for twenty galaxies drawn at random from our sample are shown in Figure 6.

In addition to our canonical  $n_b = 4$  bulge + disk fitting model (denoted as “n4” hereafter), we used two other fitting models for comparison. The first additional model was a free  $n_b$  bulge + disk model (denoted as “fn” hereafter) with  $n_b$  allowed to vary from 0.5 to 8, and the second one was a single component, pure Sérsic model (denoted as “pS” hereafter). The fitting parameters of the latter were  $F_g$ ,  $F_r$ ,  $r_e$ ,  $e$ ,  $\phi_b$ ,  $(dx)_g$ ,  $(dx)_r$ ,  $(dy)_g$ ,  $(dy)_r$  and  $n_g$  where  $n_g$  is now the global galaxy Sérsic index, and  $n_g$  was also allowed to vary from 0.5 to 8. All of these additional fits were performed with the same object deblending and sky background level as the “SIM+SEXTDEBL+GM2DSKY” dataset described above. Structural parameters from all three fitting models are compared in Section 4.2 and given in the data tables in Section 4.3.

All of our galaxy model fluxes were converted to SDSS magnitudes using:

$$m_{\text{galaxy}} = -2.5 \log_{10}(F/t) - \chi \sec z - m_0 \quad (1)$$

where  $F$  is the model flux,  $t$  is the exposure time of the SDSS corrected images (53.907456 seconds),  $\sec z$  is the airmass,  $\chi$  is the extinction coefficient, and  $m_0$  is the magnitude zeropoint. Values for these coefficients were taken directly from the SDSS database table `Field` and applied on a field-by-field basis. The photometric coefficients from this table put our flux measurements on the SDSS  $ugriz$  magnitude system. We did not transform our magnitudes from the SDSS to the AB system. The largest offset between the two systems is found in the  $u$ -band where  $u_{AB} = u_{SDSS} - 0.04$ . The offsets in the other bands are all 0.01 mag or less.

### 3.5. Rest-Frame Quantities

All angular sizes were converted to physical sizes according to the equation:

$$R = r \frac{c}{1000 H_0} \frac{1}{1+z} \int_0^z \frac{dz'}{\sqrt{\Omega_m(1+z')^3 + \Omega_\Lambda}} \quad (2)$$

where  $z$  is the redshift,  $c$  is the speed of light,  $r$  is the measured angular size in radians, and  $R$  is the corresponding physical size in kiloparsecs. Equation 2 is only valid for flat ( $\Omega_k \equiv 1 - \Omega_m - \Omega_\Lambda = 0$ ) cosmologies.

The  $g$ -band and  $r$ -band galaxy, bulge and disk rest-frame absolute magnitudes were computed from the

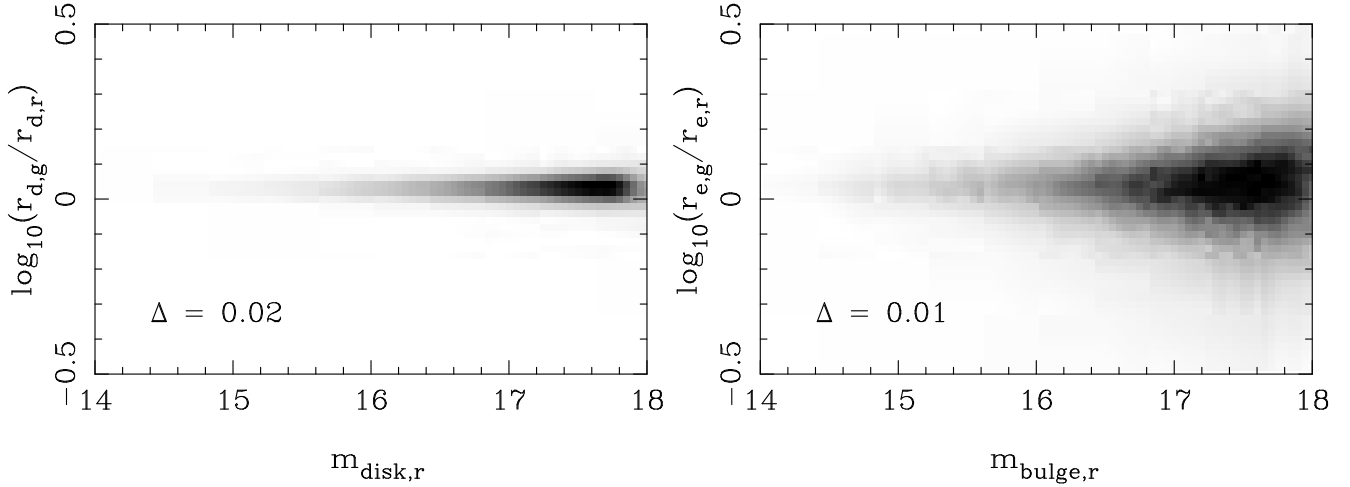


**Figure 4.** *Left-hand panel:* Log ratio of  $g$ - to  $r$ -band disk scale lengths measured from separate bandpass fits as a function of disk magnitude for galaxies with  $r$ -band bulge fraction  $(B/T)_r \leq 0.5$  and apparent half-light radius  $\geq 2''$ . The average ratio of the two disk scale lengths is  $10^{0.02} = 1.05$ . *Right-hand panel:* Log ratio of  $g$ - to  $r$ -band bulge effective radii measured from separate bandpass fits as a function of bulge magnitude for galaxies with  $r$ -band bulge fraction  $(B/T)_r > 0.5$  and apparent half-light radius  $\geq 2''$ . The average ratio of the two bulge effective radii is  $10^{0.01} = 1.02$ .

GIM2D apparent magnitudes according to the equations:

$$M_{g,g} = m_{g,g} - e_g - DM(z) - k_g \quad (3a)$$

$$M_{r,g} = m_{r,g} - e_r - DM(z) - k_r \quad (3b)$$

$$M_{g,b} = m_{g,g} - e_g - 2.5 \log_{10}((B/T)_g) - DM(z) - k_g \quad (3c)$$

$$M_{r,b} = m_{r,g} - e_r - 2.5 \log_{10}((B/T)_r) - DM(z) - k_r \quad (3d)$$

$$M_{g,d} = m_{g,g} - e_g - 2.5 \log_{10}(1 - (B/T)_g) - DM(z) - k_g \quad (3e)$$

$$M_{r,d} = m_{r,g} - e_r - 2.5 \log_{10}(1 - (B/T)_r) - DM(z) - k_r \quad (3f)$$

where  $m_{g,g}$  and  $m_{r,g}$  are the  $g$ -band and  $r$ -band observed GIM2D galaxy model magnitudes from Equation 1,  $e_g$  and  $e_r$  are the line-of-sight galactic extinctions in magnitude from the SDSS database,  $(B/T)_g$  and  $(B/T)_r$  are the GIM2D observed bulge fractions,  $DM(z)$  is the distance modulus for redshift  $z$ , and  $k_g$  and  $k_r$  are the  $k$ -corrections. The  $k$ -corrections were computed using `kcorrect` version 4 (Blanton & Roweis 2007). Rest-frame magnitudes are included in the data table presented in Section 4.3.

### 3.6. Sample Volume Corrections

Volume corrections must be applied to galaxies in our sample to properly account for the effects of selection on the visibility of different classes of galaxies. The SDSS spectroscopic sample is complete down to a  $r$ -band magnitude of 17.77 and an effective surface brightness  $\mu_{50,r}$  of 23 mag arcsec $^{-2}$  (corrected for Galactic extinction). Our  $V_{max}$  corrections are similar to the ones in Shen et al. (2003). First, the magnitude range  $r_{min} \leq r \leq r_{max}$  corresponds to a maximum redshift  $z_{max,m}$  and a minimum redshift  $z_{min,m}$ :

$$d_L(z_{max,m}) = d_L(z) 10^{-0.2(r-r_{max})} \quad (4a)$$

$$d_L(z_{min,m}) = d_L(z) 10^{-0.2(r-r_{min})} \quad (4b)$$

where  $d_L(z)$  is the luminosity distance at redshift  $z$ . The surface brightness limit constrains  $V_{max}$  for a given galaxy mainly through the  $(1+z)^4$  dimming effect. The maximum redshift at which a galaxy of surface brightness  $\mu_{50,r}$  at  $z$  can still be detected within a limiting surface brightness  $\mu_{lim} = 23$  is given by:

$$z_{max,\mu} = (1+z) 10^{(23.0 - \mu_{50,r})/10} - 1 \quad (5)$$

One difference between the  $V_{max}$  corrections in Shen et al. (2003) and the ones used here is that we do not impose a minimum size limit to galaxies in our sample. The real maximum and minimum redshifts,  $z_{max}$  and  $z_{min}$ , for a given galaxy are therefore:

$$z_{min} = \max(z_{min,m}, 0.005) \quad (6a)$$

$$z_{max} = \min(z_{max,m}, z_{max,\mu}) \quad (6b)$$

With the above limits,  $V_{max}$  is then given by the integral:

$$V_{max} = \frac{1}{4\pi} \int d\Omega f(\theta, \phi) \int_{z_{min}(\theta, \phi)}^{z_{max}(\theta, \phi)} \frac{d_A^2(z)}{H(z)(1+z)} dz \quad (7)$$

where  $H(z)$  is the Hubble parameter at redshift  $z$ ,  $c$  is the speed of light,  $f(\theta, \phi)$  is the sampling fraction as a function of position on the sky, and  $\Omega$  is the solid angle. We take the function  $f(\theta, \phi)$  to be a constant over the entire 8032 square degree areal coverage of the SDSS DR7 Legacy survey. The angular part of Equation 7 thus becomes  $(1/4\pi)(8032/41253)(4\pi) = 0.1947$ .  $V_{max}$  values are given in the data table presented in Section 4.3.

## 4. RESULTS

### 4.1. Quality Assessment

We based the quality assessment of our measured structural parameters on three science-motivated metrics.

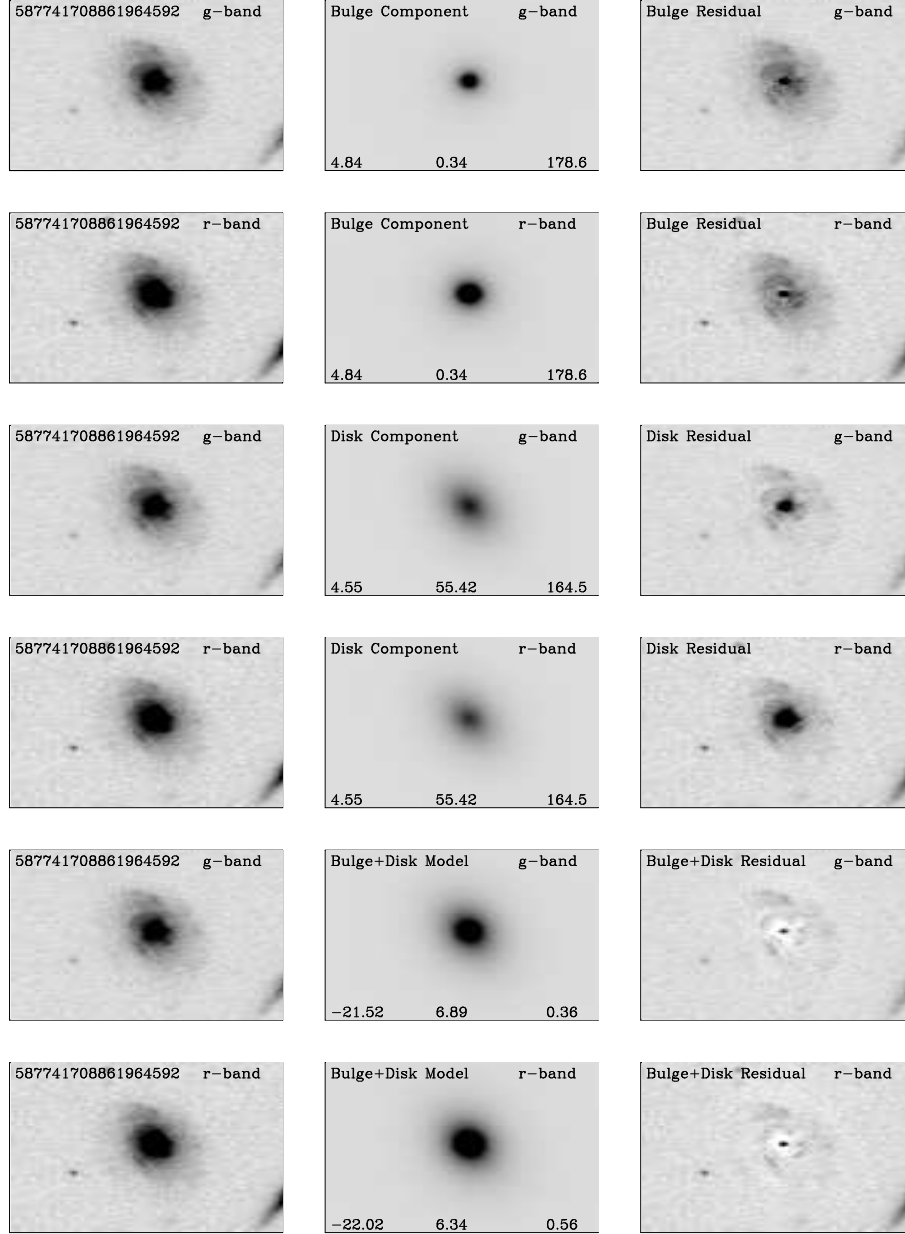


**Figure 5.** Example of a GIM2D bulge+disk decomposition (SDSS objID = 587741708861964592). From left to right: Galaxy cutout from SDSS corrected image, GIM2D output model image and GIM2D residual image. The top two rows show the bulge component only, the middle two rows show the disk component only, and the bottom two rows show the full bulge+disk model. The labels at the bottom of the bulge component images are effective radius in kiloparsecs, ellipticity ( $\equiv 0$  for circular) and position angle (measured clockwise from +y axis). The labels at the bottom of the disk component images are disk scale length in kiloparsecs, inclination angle ( $\equiv 0$  for face-on) and position angle (measured clockwise from +y axis). The labels at the bottom of the bulge+disk model images are rest-frame absolute magnitude, radius in kiloparsecs and bulge fraction. The minimum and maximum values for the greyscale stretch are  $\langle \text{bkg} \rangle - 5\sigma_{\text{bkg}}$  and  $\langle \text{bkg} \rangle + 30\sigma_{\text{bkg}}$  respectively where  $\langle \text{bkg} \rangle$  and  $\sigma_{\text{bkg}}$  are the mean and dispersion of the background pixel values.

#### 4.1.1. Size-Luminosity Relation of Disks

Figure 7 shows the size-luminosity of disks in the  $g$ -band. Disks are expected to follow a well-defined and well-known scaling relation, and most of the disks do follow such a relation. However, some disks in the “SEP+SDSSDEBL+SDSSBKG” photometric dataset lie on an “upper branch” of large disks that appear to be 2-3 times larger at a given disk luminosity. Plotting the same relation for the  $u$ -band showed an increasing bimodality in the sizes of disks. Visual inspection of these apparently large disks showed that they were in

fact caused by constant sky background residuals left after subtracting the SDSS sky values. As explained in Section 3.3, our initial procedure assumed that the SDSS sky values were “perfect” and that the GIM2D fits could be performed by fixing the sky value to zero once the SDSS sky values had been subtracted from the input science images. These constant positive sky residuals were being fit by the algorithm with a very large (and thus very flat) disk component. The false disks lie on a linear relation because of the strong covariance between luminosity and size errors through the relation

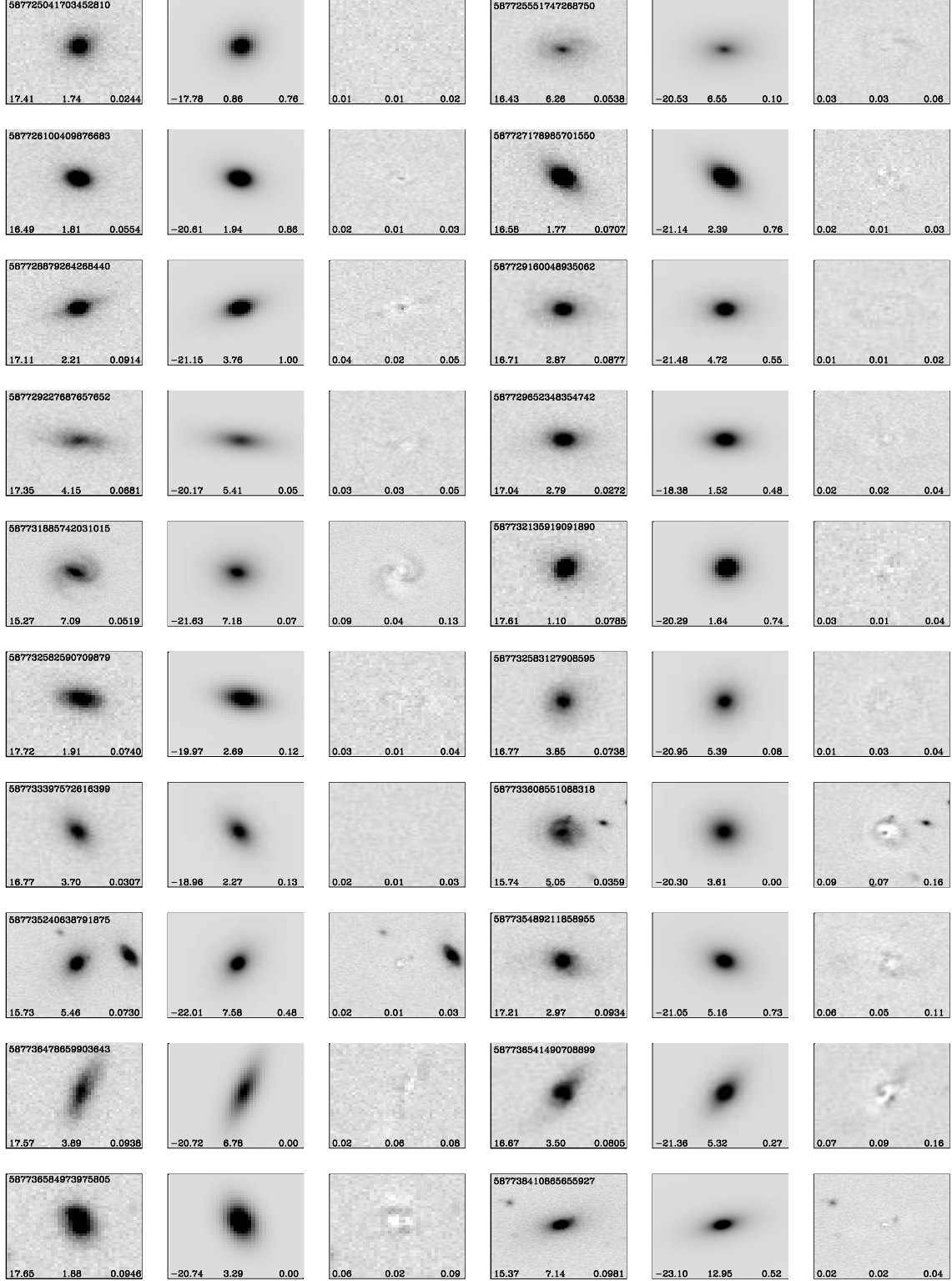


**Figure 6.** Mosaic of  $r$ -band GIM2D bulge+disk decompositions. Three postage stamp images are shown for each galaxy: galaxy cutout from SDSS corrected image, galaxy bulge+disk GIM2D model convolved with its point-spread-function, and the GIM2D residual image. Each corrected image cutout is labelled by objID, apparent GIM2D model magnitude, GIM2D model half-light radius in arcsecs, and its SDSS redshift. Each GIM2D model image is labelled by GIM2D model rest-frame absolute magnitude, GIM2D model half-light radius in kiloparsecs and GIM2D model bulge fraction. Each GIM2D residual image is labelled by three asymmetry indices:  $RT1\_2$ ,  $RA1\_2$  and  $S2 = RT1\_2 + RA1\_2$  (as defined in Simard et al. (2002, 2009)). The minimum and maximum values for the greyscale stretch for a given galaxy are  $\langle \text{bkg} \rangle - 5\sigma_{\text{bkg}}$  and  $\langle \text{bkg} \rangle + 30\sigma_{\text{bkg}}$  respectively where  $\langle \text{bkg} \rangle$  and  $\sigma_{\text{bkg}}$  are the mean and dispersion of the background pixel values.



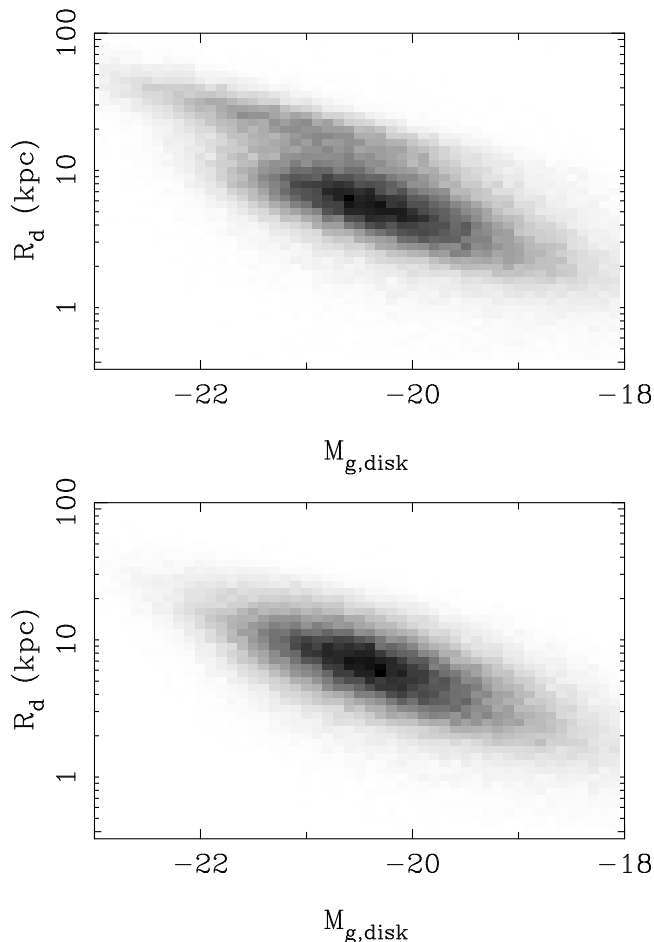


**Figure 7.** *Top panel:*  $g$ -band disk size-luminosity relation without volume corrections for face-on ( $0.75 \leq b/a \leq 1.0$ ) disks from separate fits with SDSS background levels (“SEP+SDSSDEBL+SDSSBKG”). *Bottom panel:* Same disk sample but with GIM2D-determined sky background levels (“SEP+SDSSDEBL+GM2DBKG”). Note the disappearance of the “large disks” branch with the use of GIM2D sky levels.

$F = 2\pi\Sigma_0 r_d$  for the total flux  $F$  of an exponential disk with central surface brightness  $\Sigma_0$  and scale length  $r_d$ . Recomputing local sky background levels following the procedure described in Section 3.3 corrected this problem as shown by the “SEP+SDSSDEBL+GM2DBKG” photometric dataset in the bottom panel of Figure 7. The  $u$ -band relation was also corrected by the same procedure. The disk size-luminosity relation is therefore a sensitive test of our sky background level determinations.

It is worth noting here that this sky background problem is different from the well-known problem with the photometry of bright galaxies in SDSS (Abazajian et al. 2009, and references therein). The SDSS photometric pipeline produces systematic errors in the estimation of the sky near bright ( $r < 16$ ) galaxies that cause their fluxes and scale sizes to be underestimated. The sky background problem encountered here was related to positive sky residuals. These effects of these residuals became especially significant here because sky level errors dominate the systematic errors in bulge+disk decompositions (Simard et al. 2002). It will also be more significant in more crowded environments (including close pairs of galaxies).

#### 4.1.2. Integrated Galaxy Magnitudes and Colors

Figure 8 compares our GIM2D-based total magnitudes with the SDSS Petrosian and model magnitudes as a function of bulge fraction. There are two different types of SDSS model magnitudes. The first type (called “modelMag”) comes from fitting the object with a pure deVaucouleurs and a pure exponential profile, determining which profile fits the object better and computing the magnitude of this profile. The “modelMag” magnitudes are widely used throughout the literature because they are the ones explicitly given in the SDSS database. The second type of model magnitudes (called “cmodel”) is computed from the composite flux given by the linear combination of the two profiles, i.e.,  $F_{\text{composite}} = (\text{fracDev})F_{\text{dev}} + (1 - \text{fracDev})F_{\text{exp}}$  (the value of  $\text{fracDev}$  is stored in the SDSS database). Although it would be more fair to compare the GIM2D magnitudes to the “cmodel” magnitudes, we decided to compare our photometry with the most widely used set of SDSS model magnitudes to emphasize that the use of SDSS model magnitudes requires some caution for galaxies of intermediate morphological types. This is obvious from looking at the panels in the first column of Figure 8. These panels do not depend on any GIM2D photometry. They show a “bifurcation” at intermediate bulge fraction values because the “modelMag” model magnitudes can only come from either a pure disk or a pure bulge model, and some objects with a mixture of bulge and disk components become ambiguous enough to such a binary classification that they end up in different bins.

The second and third columns of Figure 8 show that the offset between GIM2D and SDSS magnitudes is independent of bulge fraction. This lack of dependence on the type of galaxy light profiles makes it easier to compare the different sets of magnitudes. Blanton et al. (2003) reported a systematic trend between their Sérsic-based magnitude and SDSS Petrosian magnitudes as a function of the Sérsic index value with Petrosian magnitudes underestimating the  $g$ - and  $r$ -band fluxes by 20% in their high ( $n \simeq 4$ ) Sérsic index galaxies. The bifurcation at intermediate bulge fractions is also visible in the comparison between GIM2D and SDSS model magnitudes.

Object deblending can have a significant impact on galaxy photometry especially in crowded environments (Section 3.2). The simplest case of a crowded environment is a close pair of galaxies, and we tested our GIM2D photometry using the galaxy pair sample of Patton et al. (2011). This galaxy pair sample also comes with a control sample matched in stellar mass and redshift, and we used this control sample for a comparison between crowded and non-crowded environments. The control sample provides a cleaner comparison than the entire SDSS sample in the sense that selection effects due to galaxy properties such as luminosity and morphological type and technical considerations such as fiber collision are the same for both samples. Figures 9 and 10 show color-magnitude diagrams for the Patton et al. galaxy pair and control samples. These diagrams are shown for different types of photometry. The GIM2D separate fits (“SEP+SDSSDEBL+SDSSBKG”) produce a red sequence and a blue cloud that are less well-defined than those based on Petrosian and model magnitudes. GIM2D

magnitudes are *total* magnitudes in the sense that the fluxes in the best-fit bulge and disk components are integrated to infinity, and as such, they will have a lower signal-to-noise ratio than Petrosian magnitudes, say, that aim to minimize the amount of missing flux while optimizing the signal-to-noise ratio of the photometric measurements. The GIM2D fits also yield a large number of bright galaxies over the range  $-24 \leq M_r \leq 21$ . As discussed in Section 4.1.1, the GIM2D-determined sky backgrounds yielded better disk sizes and luminosities. Adopting this new background level determination method also decreases the number of those bright outliers, but significant scatter towards bluer and redder colors remains.

Switching from bulge+disk fits performed separately in each filter to the ones performed simultaneously in both bandpasses immediately improves the integrated magnitudes in two important ways. The number of blue and red outliers is now significantly lower, and the red sequence and blue cloud are now as well-defined as for the SDSS photometry. The simultaneous fits produce smaller errors because they simultaneously make use of all the data available for a given object. Visual inspection of the remaining outliers showed them to be in crowded environments where the SDSS object deblending was failing. Adopting the SExtractor deblending (in addition to the simultaneous fits) described in Section 3.2.2 eliminated nearly all of the remaining outliers to produce a very clean color-magnitude diagram. The lack of red outliers in the final GIM2D color-magnitude diagram is especially noteworthy. As explained in Patton et al. (2011), the presence of these outliers in the official SDSS photometry was ascribed in the literature to a new population of extremely-red pair galaxies (e.g., Alonso et al. 2006; Perez et al. 2009; Darg et al. 2010). The GIM2D photometry given here shows that they are in fact due to crowding errors from incorrect deblending. The crowding errors in SDSS preferentially scatter galaxy colors towards the red for the following reason. The  $r$ -band images go deeper in surface brightness than the  $g$ -band ones because the SDSS detectors are more red sensitive. The outer isophotes of two neighboring galaxies will therefore overlap more in the red than in the blue, and the SDSS deblender will leave more faint isophotal light behind in the red. When this residual light for a galaxy is included in the photometry of its neighbor(s), it yields (a) redder neighbor galaxy color(s).

#### 4.1.3. Fiber Colors

Our third data quality metric is based on fiber apparent magnitudes and colors. The fiber magnitude of a given object is computed from the flux measured within the aperture of a spectroscopic fiber. The diameter of this aperture is  $3''$ . The fiber magnitudes are given in the SDSS database. Given the apparent sizes of the SDSS galaxies with respect to this fiber aperture, fiber magnitudes (and colors) are most often measurements of the central part of a galaxy. The typical fiber covering fraction, which is the ratio of the  $g$ -band Petrosian to fiber fluxes, is 30% (Ellison et al. 2008). We can also compute fiber magnitudes from the GIM2D output model images for comparison with the SDSS fiber quantities. The fiber aperture on the GIM2D model images was centered on the SDSS position of the galaxy

on the sky ( $(dx, dy) = (0, 0)$ ) and not on the center of the GIM2D model itself which was allowed to move for the fits. Using the SDSS and GIM2D fiber magnitudes, we then computed a  $\Delta(\text{fiber color})$  given by  $(g-r)_{\text{gim2d, fiber}} - (g-r)_{\text{SDSS, fiber}}$ . This  $\Delta(\text{fiber color})$  is plotted in Figure 11 as a function of projected galaxy-galaxy separation on the sky for galaxies in the pair sample of Patton et al. (2011). The median  $\Delta(\text{fiber color})$  value is not zero due to PSF effects. The SDSS fiber magnitudes were computed by uniformly convolving all the SDSS images to a  $2''$  seeing whereas the typical size of the SDSS PSFs used for the GIM2D model images is  $1''.4$  FWHM. This narrower PSF FWHM spreads less bulge (i.e., red) light outside of the fiber aperture thus making the GIM2D fiber colors slightly redder. A large positive or negative  $\Delta(\text{fiber color})$  indicates that a bulge+disk decomposition failed because it did not even reproduce the central parts of the galaxy. SDSS deblending produces a large number of outliers, and the number of these outliers increases with decreasing pair separation. The number of galaxies with large  $\Delta(\text{fiber color})$  values increases significantly at separations less than 20 kiloparsecs which corresponds to angular separations less than  $10''.8$  at  $z = 0.1$ . Switching to SExtractor deblending eliminates the vast majority of the outliers, and no trend is seen anymore as a function of pair separation. This is another example where SExtractor deblending produces more reliable photometry in crowded environments.

## 4.2. Galaxy Fitting Models

### 4.2.1. Selecting the Appropriate Model with the $F$ -Statistic

It is not always true that a galaxy will be appropriately modelled by a multi-component photometric model; in instances where galaxies are best represented by a pure bulge or disk or, alternatively, the data cannot support a more complex model decomposition due to low signal-to-noise or poor spatial sampling, it is unclear how to treat the output of our “n4” or “fn” fits. We therefore want a way to assess the appropriateness of different model decompositions, and a means of deciding when a complex model, e.g. bulge+disk, is to be preferred over a pure Sérsic profile. We approach this question of finding the appropriate fitting model using the  $F$ -test to compare the  $\chi^2$  residuals of our “pS”, “n4”, and “fn” fits (see Section 3.4). The  $F$ -test provides a quantitative means of judging the relative likelihood of different structural decompositions. There are of course other approaches (e.g., Allen et al. 2006), but the  $F$ -test seems to be a powerful and straightforward approach as we show below. For each model we estimate the reduced  $\chi^2$  using the fit residuals and the number of resolution elements per fit,  $n_{\text{res}}$ , in this instance estimated as  $n_{\text{res}} = n_{\text{pixels}}/(\pi\Theta^2)$ , where  $n_{\text{pixels}}$  is the number of unmasked (object) pixels used in the fit and  $\Theta$  is the  $r$ -band seeing half-width at half maximum (HWHM) in pixels. The computed  $F$  values for a given pair of models, e.g. “fn” vs. “pS”, can then be translated into a corresponding probability that a smaller  $F$  would be observed under the null hypothesis that a galaxy is similarly well fit by the two decompositions (i.e. that their rms flux residuals are comparable); these probabilities are given in Tables 1 and 2. In a given table, we only provide the probability relative to less complex models, such that the probabilities always

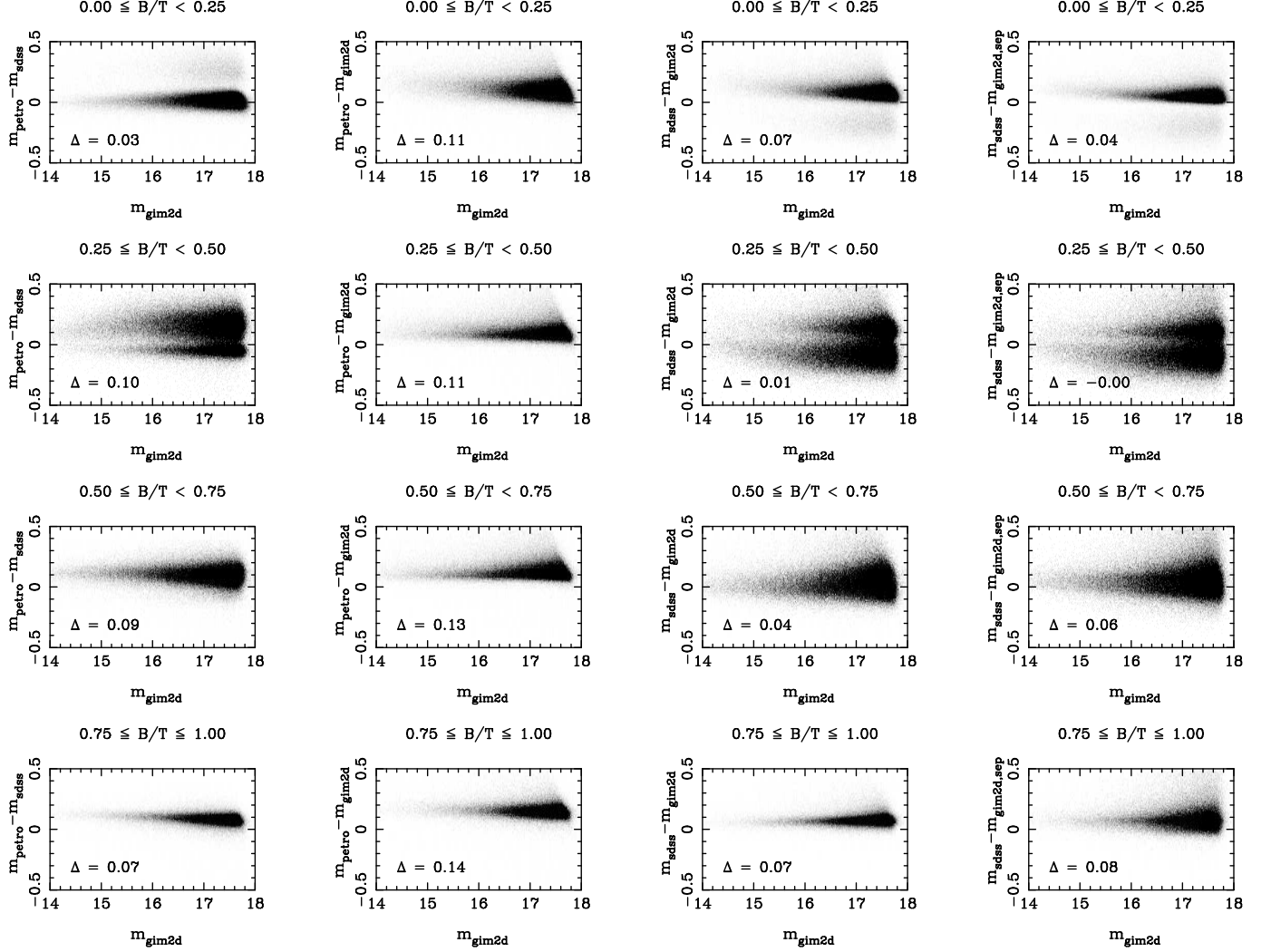


**Figure 8.** Comparison of  $r$ -band GIM2D magnitudes with Petrosian and model SDSS magnitudes (“modelMag”) as a function of  $r$ -band bulge fraction. *First column:* SDSS Petrosian versus SDSS model. *Second column:* SDSS Petrosian versus GIM2D (“SIM+SEXTDBL+GM2DBKG”). *Third column:* SDSS model versus GIM2D (“SIM+SEXTDBL+GM2DBKG”). *Fourth column:* SDSS model versus GIM2D (“SEP+SDSSDBL+SDSSBKG” denoted  $m_{\text{gim2d,sep}}$  here). Note that the panels in the first column do not depend on any GIM2D photometry.

correspond to the lower-tail probability of the appropriate  $F$ -distribution. In other words,  $P_{pS}$  is the probability that a bulge+disk model is *not* required (compared to a pure Sérsic model), and  $P_{n4}$  is the probability that a free  $n_b$  bulge + disk model is *not* required (compared to a fixed  $n_b = 4$  bulge + disk model).

The distributions of  $F$ -test probabilities versus bulge fraction are shown in Figure 12, and they bring forth the limitations of the SDSS imaging in terms of spatial resolution and signal-to-noise. A bulge+disk model is clearly required for galaxies with  $0.2 \leq (B/T)_{fn} \leq 0.45$ , and galaxies with  $(B/T)_{fn} > 0.75$  do not require a bulge+disk model to fit their light profiles. If we set a value of  $P_{pS} \leq 0.32$  as the ( $1\sigma$ ) threshold below which galaxies are likely to be genuine bulge+disk systems, then the fraction of these galaxies in our entire SDSS sample is 26%. The quality of the SDSS imaging is insufficient to determine bulge Sérsic indices for galaxies in our selected range of apparent magnitudes as  $P_{n4}$  versus

bulge fraction does not show any statistically significant differences between  $n_b = 4$  and free  $n_b$  models. Only 9% of the galaxies have  $P_{n4} \leq 0.32$ .

Figure 13 illustrates the usefulness of the  $F$ -test probabilities to select genuine bulge+disk systems. The axial ratio distribution of a sample of disks randomly inclined in space should be uniform between zero and one modulo some perturbations due to dust and/or bars. Looking at the top row of Figure 13, one can see that the observed distribution is indeed uniform at low bulge fraction, but that it also tends towards the same axial ratio distribution as bulges towards higher bulge fractions if no  $F$ -test selection is made. This behavior would argue that “disks” in highly bulge-dominated galaxies are not in fact real but were rather introduced by the fitting algorithm as an additional degree of freedom to model the outer wings of a single component galaxy. If we select only galaxies with  $P_{pS} \leq 0.32$ , then one can see that the resulting disk axial ratio remains uniform even at the

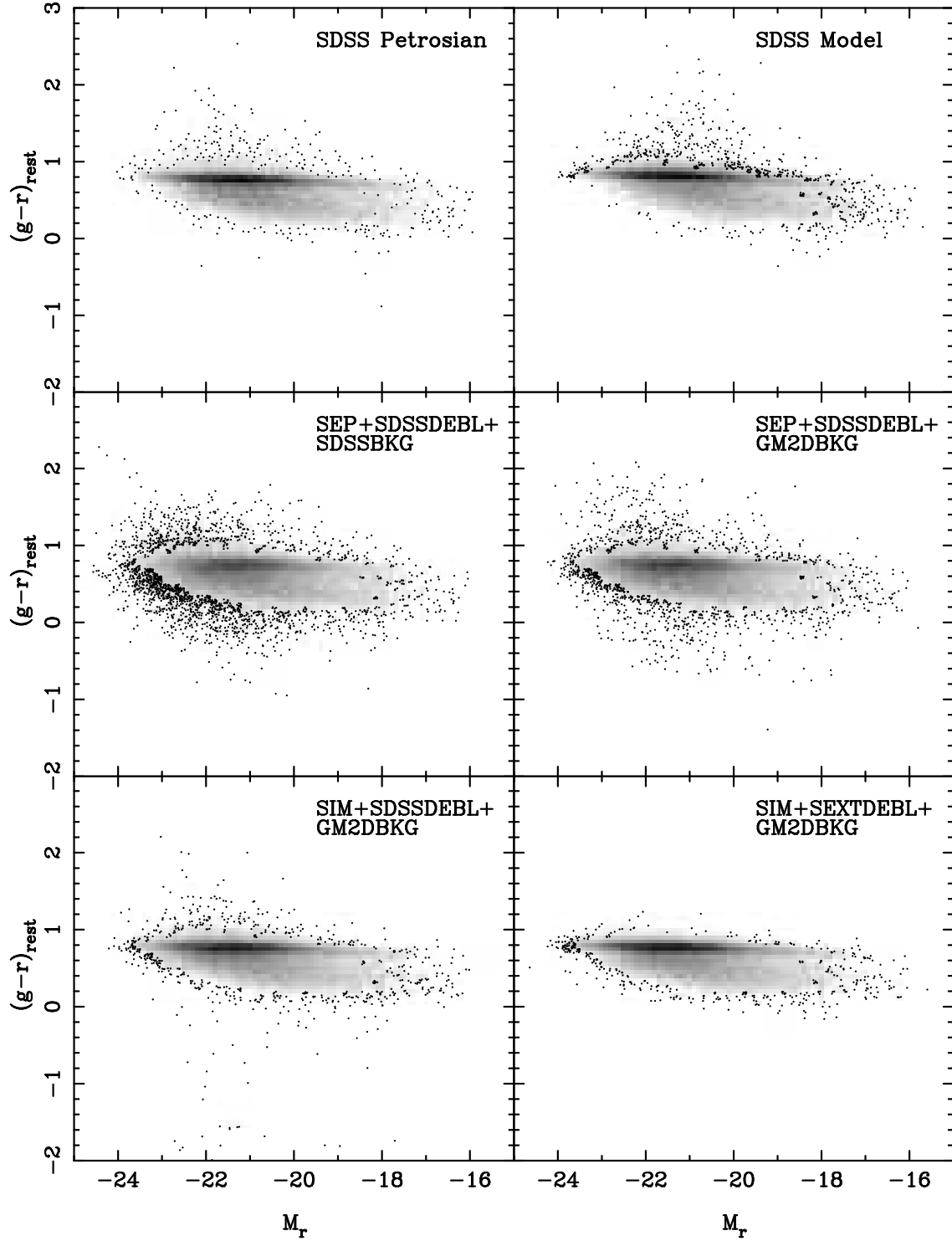


**Figure 9.** Comparison of rest-frame color-magnitude diagrams for the Patton et al. (2011) DR7 galaxy pair sample of ( $N=22565$ ): *Top left:* SDSS Petrosian magnitudes *Top right:* SDSS model magnitudes *Middle left:* GIM2D separate fits with SDSS sky background and deblending, *Middle right:* GIM2D separate fits with GIM2D sky background and SDSS deblending *Bottom left:* GIM2D simultaneous fits with GIM2D sky background and SDSS deblending. *Bottom right:* GIM2D simultaneous fits with GIM2D sky background and SExtractor deblending. The same greyscale was used in all subpanels. The bin size for the greyscale was  $(\Delta(g-r), \Delta M_r) = (0.1, 0.05)$ . The greyscale was replaced by the actual data points wherever the number of points in a given bin was less than 2.

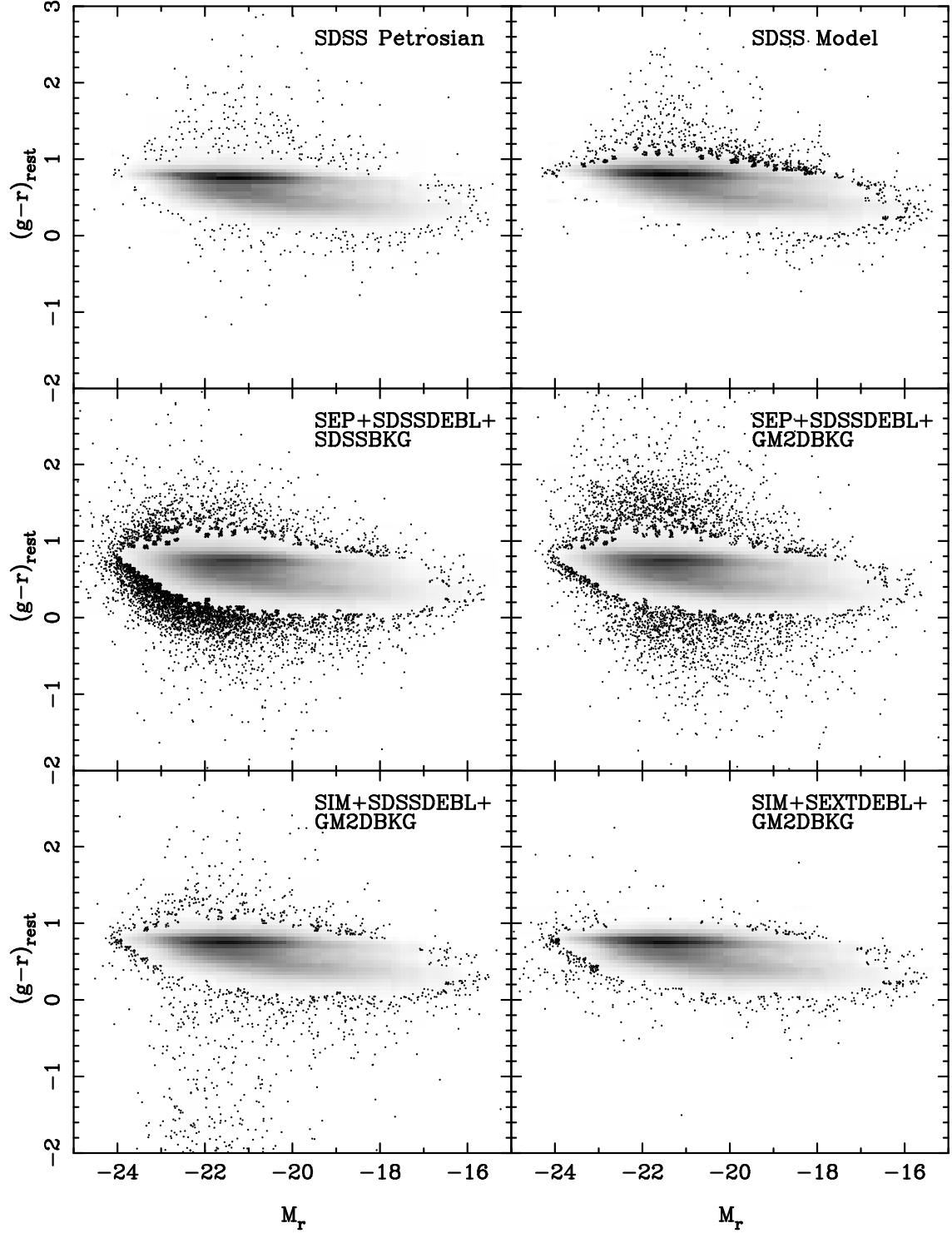


**Figure 10.** Comparison of rest-frame color-magnitude diagrams for the Patton et al. (2011) DR7 galaxy pair control sample ( $N=290090$ ): (Top left) SDSS Petrosian magnitudes, (top right) SDSS model magnitudes, (middle left) GIM2D separate fits with SDSS sky background and deblending, (middle right) GIM2D separate fits with GIM2D sky background and SDSS deblending, (bottom left) GIM2D simultaneous fits with GIM2D sky background and SDSS deblending, and (bottom right) GIM2D simultaneous fits with GIM2D sky background and SExtractor deblending. The same greyscale was used in all subpanels. The bin size for the greyscale was  $(\Delta(g-r), \Delta M_r) = (0.1, 0.05)$ . The greyscale was replaced by the actual data points wherever the number of points in a given bin was less than 2.

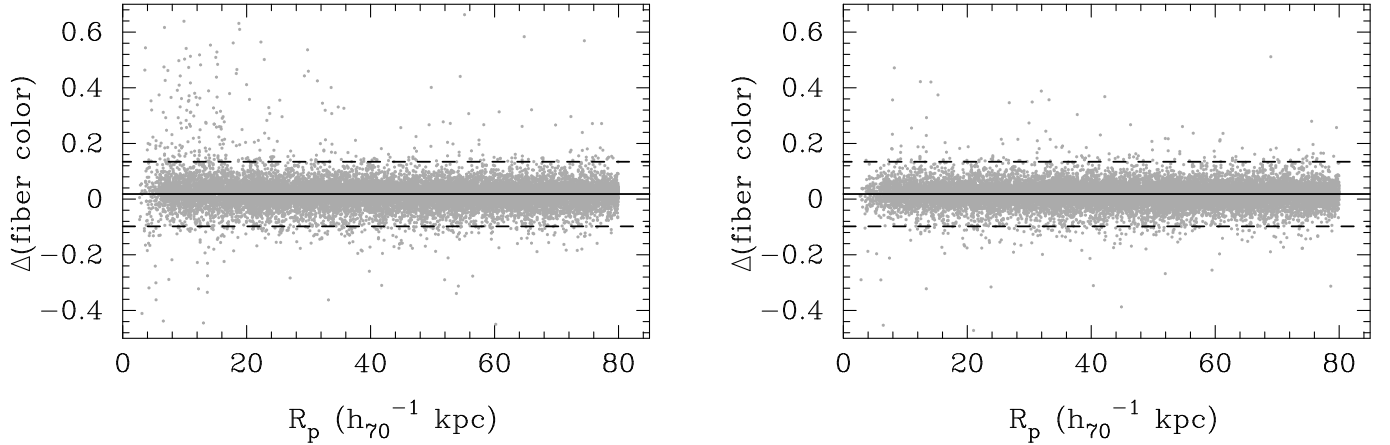


**Figure 11.**  $\Delta(\text{fiber color})$  as a function of galaxy pair separation in kiloparsecs with SDSS deblending (*left-hand panel*) and SExtractor deblending (*right-hand panel*).  $\Delta(\text{fiber color})$  is defined as  $(g-r)_{\text{gim2d, fiber}} - (g-r)_{\text{SDSS, fiber}}$ . The lines show the median fiber color (solid line, median value = 0.0182) from SDSS deblending and the  $1-\sigma$  envelope (dashed lines,  $\sigma = 0.116$ ). The same lines are reproduced in both panels. Note the excess of outliers in the left panel at small separations due to poor deblending.

highest bulge fractions. We are thus able to select real disks in highly bulge dominated galaxies.

#### 4.2.2. Structural Parameter Comparison

A detailed comparison between our three different fitting models could easily stand on its own as a separate paper, so we briefly comment here on the salient points of this comparison. We start by looking at measurements of the global galaxy structure from the different models namely the galaxy Sérsic index  $n_g$  and the bulge fraction  $B/T$ . The distribution of galaxy Sérsic index values in Figure 14 shows a sharp peak at  $n_g = 0.5$ , a broader and larger peak at  $n_g = 1$ , no peak at  $n_g = 4$  and a peak at the maximum allowed Sérsic value of 8. We will return to the peaks at  $n_g = 0.5$  and  $n_g = 8$  later. The large peak at  $n_g = 1$  reflects the fact that the local galaxy population is dominated by disk galaxies. The lack of a strong peak at  $n_g = 4$  is quite interesting because it argues for a lack of global structural similarity in galaxies that are not disk-dominated. In terms of bulge fraction, measured values from both the  $n_b = 4$  and free  $n_b$  fits (denoted as  $(B/T)_{n4}$  and  $(B/T)_{fn}$  respectively here) are well correlated with one another and with  $n_g$  (Figure 14).  $(B/T)_{n4}$  and  $(B/T)_{fn}$  increase with  $n_g$  and reach a value of one at  $n_g = 4$ . Two “branches” are seen beyond  $n_g = 4$ : one at  $B/T \sim 1$  and another one at  $B/T \sim 0.5$ . The first branch is not surprising, but the second one may point to a potential single- versus double-component degeneracy in the bulge+disk decompositions. In order to understand the behavior of  $(B/T)$  at high  $n_g$ , we looked at the bulge and disk ellipticity difference  $\Delta e \equiv e_b - e_d$  versus the ratio of the bulge and disk half-light radii  $R_{b/d} \equiv r_e/(1.67r_d)$  in the range  $7 \leq n_g < 8$  for two ranges in  $(B/T)_{n4}$ :  $0.4 \leq (B/T)_{n4} \leq 0.7$  and  $0.9 \leq (B/T)_{n4} < 1.0$ .  $\Delta e$  is zero which means that the bulges and disks have the same ellipticities i.e., these galaxies may actually have a single component but the fitting algorithm may be using a bulge and disk components to model something that it cannot do even with  $(B/T)_{n4} = 1$  for  $n_b = 4$ . The dichotomy actually comes from the ratio of the radii. Galaxies with  $0.4 \leq (B/T)_{n4} \leq 0.7$  all have  $R_{b/d}$  values of 0.13 with a dispersion of 0.05 whereas galaxies with  $0.9 \leq (B/T)_{n4} < 1.0$  have values around 0.56 with a dis-

persion of 0.16. There are six times more galaxies with  $0.4 \leq (B/T)_{n4} \leq 0.7$  than with  $0.9 \leq (B/T)_{n4} < 1.0$ . The peak in  $R_{b/d}$  where a galaxy ends up seems to depend on the spread in  $\Delta e$ . The dispersion in  $\Delta e$  for galaxies with  $0.4 \leq (B/T)_{n4} \leq 0.7$  is twice the dispersion in  $\Delta e$  for galaxies with  $0.9 \leq (B/T)_{n4} < 1.0$ . A smaller  $\Delta e$  value for a given galaxy makes it more likely that the fitting algorithm will tend towards a single component model rather than a two-component model because the algorithm will need two components to model a change of ellipticity with radius that does not come from PSF smearing. There is no significant difference between  $(B/T)_{n4}$  and  $(B/T)_{fn}$  as a function of bulge Sérsic index except at very low values of  $n_b \simeq 0.5$  where  $(B/T)_{n4}$  can be considerably lower than  $(B/T)_{fn}$  (Figure 14). This behavior at low  $n_b$  is expected given that trying to fit a bulge with a very flat profile using a relatively peaky  $n_b=4$  component will force the algorithm to minimize the contribution of this  $n_b=4$  component as much as possible by converging to a very low bulge fraction. Some previous studies (e.g., Graham & Worley 2008) have reported a dependence of  $(B/T)$  on  $n_b$ . Such a dependence is not seen here, but this may be due to the lack of constraint on bulge profile shape from the SDSS images of the galaxies in our sample as discussed next.

The choice of a Sérsic index value for the galaxy bulge profile has long been debated in the literature (Andredakis et al. 1995; de Jong 1996; Balcells et al. 2003; Kormendy & Kennicutt 2004; Fisher & Drory 2010; Laurikainen et al. 2010), and our very large sample of free  $n_b$  + disk decompositions should at first glance offer some insight on this interesting question. However, the vast majority of the galaxies in our sample have images that do not have the required spatial resolution and/or signal-to-noise ratio (Section 4.2.1 and Figure 12). If we select galaxies for which both  $P_{pS}$  and  $P_{n4}$  are less or equal to 0.32, then we obtain a subsample of almost 53,000 galaxies for which we have good enough images to study their bulge profile shape. Figure 15 shows the distribution of  $n_b$  for this subsample. There are three important features to examine here. First, there is a peak at  $n_b = 0.5$ . We examined the distribution of galaxies with  $0.5 \leq n_b < 0.55$  in apparent bulge size  $r_e$  and bulge ellipticity  $e$ , and this distribution showed that es-

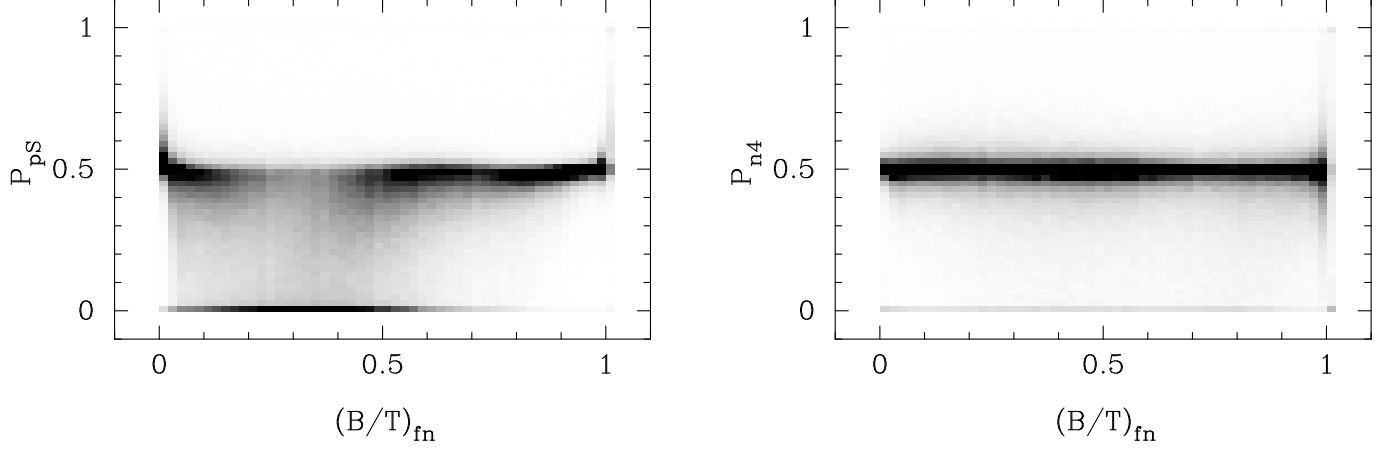


**Figure 12.**  $F$ -test probabilities  $P_{PS}$  (left panel) and  $P_{n4}$  (right panel) versus bulge fraction for the free  $n_b$  bulge + disk decompositions. The greyscale represents the two-dimensional distribution of galaxies normalized by the total number of galaxies. The  $x$ -axis and  $y$ -axis bin sizes for the two-dimensional distributions were both 0.02. The limits for the greyscale go from zero to 20% of the peak value of the normalized distribution.

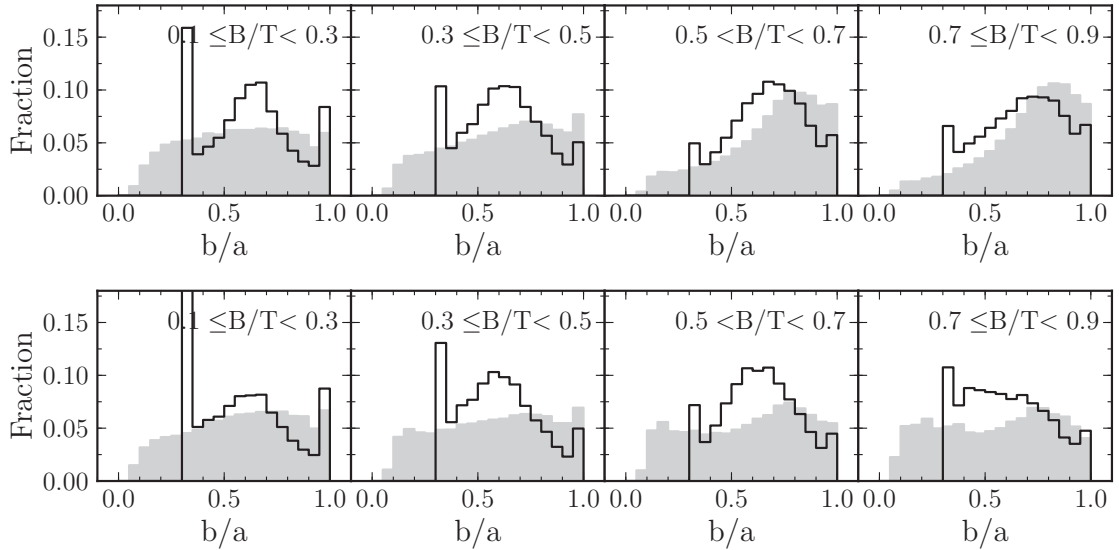


**Figure 13.** Bulge and disk axial ratio distributions for  $n_b = 4$  + disk models. In each panel, shaded and open histograms show the distribution of disk and bulge axial ratios. *Top row:* Axial ratio distribution for the full sample of  $n_b = 4$  + disk fits. Note the excess of  $b/a > 0.5$  disk components at high  $B/T$ . *Bottom row:* Axial ratio distribution for the subsample of  $n_b = 4$  + disk models where  $P_{PS} \leq 0.32$ , i.e., where galaxies are likely to be genuine bulge+disk systems. Note the significant reduction of low-inclination disks, particularly at  $B/T > 0.5$ .

entially all of these galaxies ( $N \sim 6,700$ ) were located in a peak at  $e \sim 0.7$  and  $r_e \lesssim 1''$ - $2''$ , i.e., 3-5 pixels. A combination of low  $n_b$  and high  $e$  values is expected when the fitting algorithm tries to make the bulge profile as flat and as elongated as possible to try to fit a bar or include off-center components (point sources, very close mergers, etc.). We visually inspected a subsample of galaxies in this peak using the SDSS SkyServer Object Explorer<sup>7</sup> to confirm this expectation. Second, the  $n_b$  distribution has a broad bump around  $n_b = 5.5 - 6.0$ . The de Vaucouleurs value of  $n_b = 4$  is not preferred for this subsample. However, choosing  $n_b = 4$  for the entire sample is still a reasonable choice for the following reason. When the bulge Sérsic index cannot be constrained due to spatial resolution and/or signal-to-noise limita-

tions, its posterior probability distribution (which is fully mapped by GIM2D) will be uniformly flat between the minimum and maximum allowed values. Our allowed range of values was 0.5-8 based on previous studies of the Sérsic index of spheroids. The median value of a flat posterior probability distribution (which we take to be the best-fit value) will therefore be around 4. Indeed, if we re-plot Figure 15 for the entire sample with no  $F$ -test selection, we see a very strong peak at  $n_b = 4$ , but this peak reflects a lack of constraint on bulge profile rather than its actual shape. Third, there is an upturn in the  $n_b$  distribution at  $n_b \gtrsim 7.5$ . We again examined a plot of  $r_e$  versus  $e$  for these galaxies and found peaks at  $e \sim 0$  and  $e \sim 0.7$  with a uniform distribution in sizes over the range  $r_e < 3''$ . Visual inspection of galaxies at  $e \sim 0$  and  $e \sim 0.7$  with smaller sizes ( $r_e \lesssim 0''.4$ ) showed them to have nuclear, *on-center* sources. Galaxies at  $e \sim 0$

<sup>7</sup> <http://cas.sdss.org/dr7/en/tools/explore/obj.asp>

larger sizes ( $r_e \sim 2-3''$ ) did not exhibit any distinguishing characteristic as a group, and galaxies at  $e \sim 0.7$  and larger sizes ( $r_e \sim 2-3''$ ) had a bar+point source configuration. Galaxies with low and high  $n_b$  values in Figure 15 also have low and high  $n_g$  values in Figure 14. All of these different sub-classes of objects highlight the power of comparing different fitting models to identify different types of galaxy substructures.

Galaxy half-light radii from  $n_b = 4$  and free  $n_b$  decompositions ( $r_{hl,n4}$  and  $r_{hl,fn}$  respectively) are quite consistent over the full range of allowed  $n_b$  values (Figure 16). Not surprisingly, galaxy half-light radii differ between pure Sérsic ( $r_{hl,pS}$ ) and bulge+disk fits at  $n_g > 4$  with  $r_{hl,pS}$  being 50% larger at  $n_g = 8$ . This is entirely due to the fact that the half-light radii are calculated by integrating best-fit models with different profiles in their outer wings. The bulge radii exhibit the expected shape from the well-known and strong covariance between  $n_b$  and  $r_e$ , and the choice of  $n_b$  will obviously have a significant impact on the measurements of  $r_e$ . On the other hand, it is very important to note that the disk scale length does *not* appear to be affected by the Sérsic index of the bulge for the majority (80%) of the galaxies in our sample, and that the scatter in the disk luminosity-size relation (Figure 7) therefore does not depend on the choice of bulge Sérsic index. This apparent lack of dependence of  $r_d$  on  $n_b$  may be due to the lack of constraint on bulge profile shape discussed earlier, but it may also be due to bulges being usually more compact than their disks. The covariance between measured bulge and disk parameters will be weaker in galaxies where the two components are more spatially distinct. More details on the disk luminosity-size distribution are given in Simard 2011, in preparation.

#### 4.2.3. Sérsic Model Comparison with NYU Value-Added Catalog

The New York University Value-Added Galaxy Catalog (Blanton et al. 2005a) provides Sérsic model structural parameters for galaxies in the SDSS spectroscopic sample. The details and tests of the NYU Sérsic measurements including artificial galaxy simulations are described in the appendix of Blanton et al. (2005b). We matched objects in our pure Sérsic structural catalog with objects in the NYU catalog using MJD, PLATEID and FIBERID for cross-identifications, and a match was found for 666,740 objects.

Figure 17 shows the comparison between NYU and GIM2D galaxy Sérsic half-light radii and indices. The trend in half-light radius shown in the left-hand panel is fully consistent with the NYU simulations if  $n_{g,gim2d}$  and  $r_{hl,gim2d}$  are taken to be equivalent to the input (“true”) values used for the NYU simulations ( $n_{in}$  and  $r_{50,in}$  respectively). The galaxy half-light radii from the NYU fits are smaller by about 20% than both their input simulation values and the GIM2D values for objects with  $n_g \geq 5$ . There is an offset  $\Delta n \sim 0.3-0.4$  between GIM2D and NYU Sérsic indices at  $n_g = 1$ . This offset depends on galaxy ellipticity: it increases from 0.2 at low  $e$  ( $< 0.1$ ) to 0.5 at higher  $e$  ( $> 0.4$ ). This dependence on ellipticity comes from the fact that the NYU profile fits were done on one-dimensional profiles extracted from two-dimensional images using *circular* annuli. The offset does not completely disappear even at low  $e$  possibly as a

result of the fact that the NYU fits were done on  $r$ -band images only whereas our fits were done simultaneously on  $g$ - and  $r$ -band images, and a redder band will be more dominated by the redder, spheroidal (i.e., higher Sérsic index) component of a galaxy.

The comparison between the NYU and GIM2D Sérsic parameters therefore shows good agreement given the differences in how the two sets of parameters were measured.

#### 4.3. Data Tables and Some Cautionary Notes

The data quality metrics used in Section 4.1 show that the GIM2D “SIM+SEXTDEBL+GM2DBKG” dataset gives the most robust photometric results. The photometric data for this dataset are given in Tables 1, 2 and 3 for the  $n_b = 4$  bulge + disk, the free- $n_b$  bulge + disk and the pure Sérsic decompositions respectively. Two sets of galaxy half-light radii are given in these tables. The semi-major half-light radius  $R_{hl}$  of a galaxy was calculated by individually collapsing the bulge and disk components onto their respective major axes, adding these two one-dimensional profiles into a global galaxy profile and computing the half light radius of this summed one-dimensional profile. The circular half light radius  $R_{chl}$  was computed by performing curve-of-growth photometry in circular apertures on the *intrinsic* (i.e., not PSF convolved) GIM2D best-fit model image of the galaxy. The relationship between the two kinds of half-light radius is easy to understand for a single component galaxy because it is given in this case by  $R_{chl} = R_{hl}\sqrt{1-e}$  where  $e$  is the ellipticity of this component.

The best way to use the data listed in the structural parameter tables is to consider bulges and disks as separate galaxy sub-populations overlapping on the sky. As one would expect, bulge structural parameters are more reliable for brighter bulges (Figure 18), and disk structural parameters are more reliable for brighter disks (Figure 19). The reliability of the structural parameters of a given subcomponent is largely independent of the other subcomponent (e.g., Figure 16). One should not study bulge or disk properties on the basis of a simple selection cut on bulge fraction. The bulge of a bright, low  $B/T$  galaxy can still be brighter than the bulge of a faint, high  $B/T$  galaxy. Bulge and disk subsamples should be selected on the basis of their magnitudes.

Another important note of caution is related to the use of bulge fraction cuts to select early-type galaxy subsamples. As many previous studies have shown (Im et al. 2002; McIntosh et al. 2002; Tran et al. 2003; Blakeslee et al. 2006; Simard et al. 2009), early-type galaxies should be selected using both bulge fraction *and* image smoothness. For example, a nuclear starburst in a relatively irregular galaxy would yield a high bulge fraction, and such a galaxy would be erroneously classified as an early-type if bulge fraction were the sole selection criterion. The agreement between visual and quantitative classification of galaxies has been shown to be excellent when both parameters are used (Simard et al. 2009).

Finally, internal dust should also be considered as a potential source of bias when selecting samples of bulges and/or disks for study. Disks are known to be dusty (e.g., Driver et al. 2007, and references therein), and this dust can broaden the intrinsic disk/bulge luminosity-size or luminosity-color distributions. One can deal with this



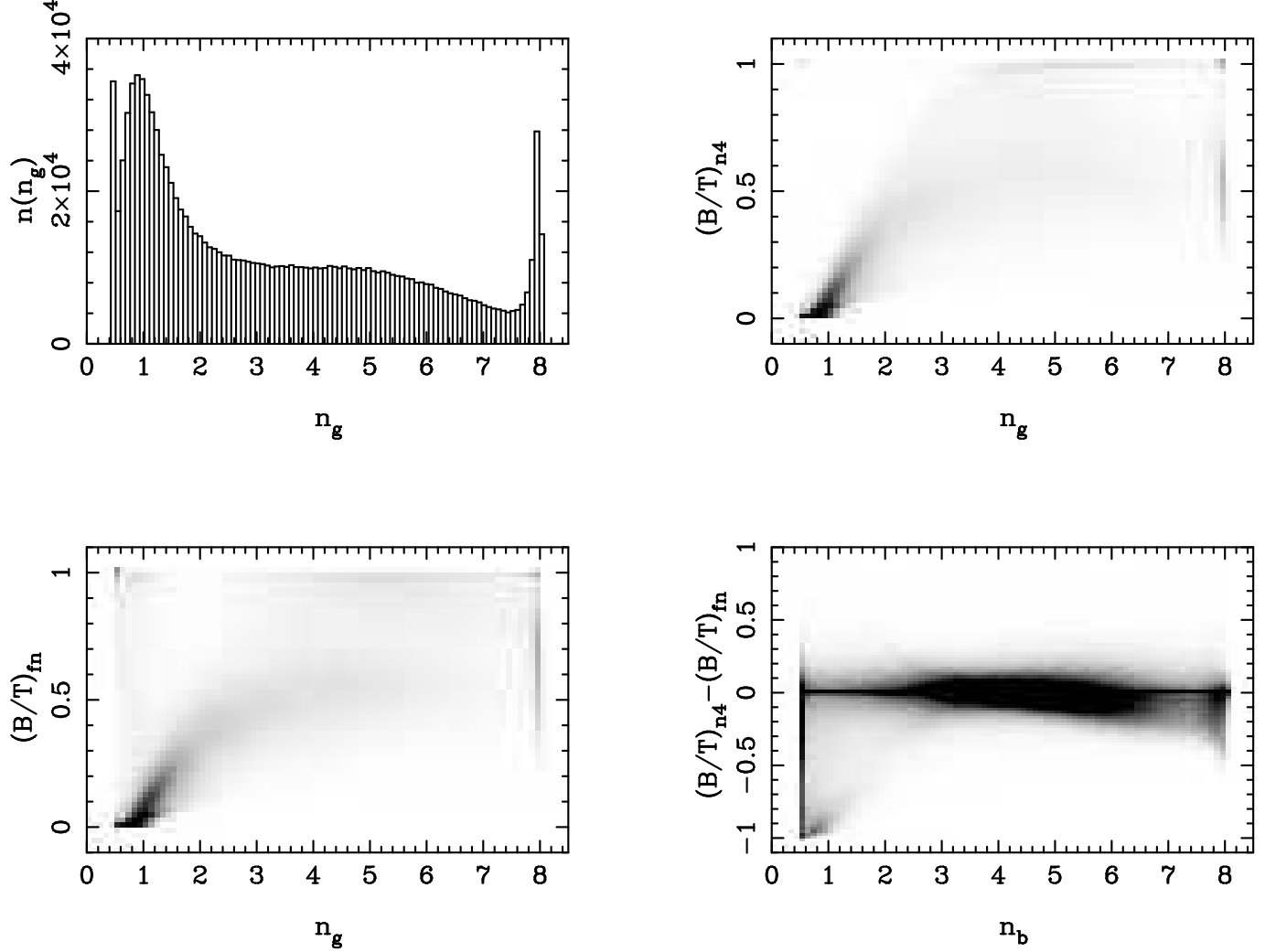


**Figure 14.**  $r$ -band GIM2D galaxy bulge fractions and Sérsic indices from the three different fitting models. *Top left:* Distribution of the galaxy Sérsic index  $n_g$  from the single component, pure Sérsic fits. *Top right:* Bulge fraction  $(B/T)_{n4}$  from the  $n_b = 4$  bulge + disk decompositions versus galaxy Sérsic index  $n_g$ . *Bottom left:* Bulge fraction  $(B/T)_{fn}$  from the free  $n_b$  bulge + disk decompositions versus galaxy Sérsic index  $n_g$ . *Bottom right:* The difference between  $(B/T)_{fn}$  and  $(B/T)_{n4}$  as a function of bulge Sérsic index  $n_b$ . The greyscale represents the two-dimensional distribution of galaxies normalized by the total number of galaxies. The bin sizes for the two-dimensional distributions were  $\Delta(n_g) = 0.1$  and  $\Delta(B/T) = 0.02$ . The limits for the greyscale go from zero to 20% of the peak value of the normalized distribution.

bias by either selecting galaxies with face-on disks or applying empirical internal dust extinction corrections. These corrections can be difficult to characterize, but the large number of galaxies included in the catalogs presented here offers the opportunity of deriving these corrections as needed by various science programs (Simard 2011, in preparation).

##### 5. SUMMARY

We have performed bulge+disk decompositions for 1.12 million galaxies in the Legacy area of the SDSS Data Release 7. Four decomposition procedures were used, and one of these procedures clearly produced more robust structural parameters, magnitude and colors when looking at three science-based data quality assurance metrics. The most reliable procedure included the following three important steps:

- GIM2D-based sky background level determination

- SExtractor object deblending
- Simultaneous bulge+disk decomposition in  $g$  and  $r$

We also used three different fitting models: a  $n_b = 4$  bulge + disk model, a free- $n_b$  bulge + disk model and a pure Sérsic model, and we provide a detailed comparison between the measured structural parameters from these fitting models with a mean to select the appropriate model for a given galaxy using the  $F$ -statistic. This comparison highlights the importance of this selection for a given science goal. Pure Sérsic model fits might be better suited to studies of global galaxy colours whereas a cut on the  $F$ -test probability  $P_{pS}$  to select galaxies for which a bulge+disk model was required would be better for studies of bulge/disk colours. Using a low cut on both  $P_{pS}$  and  $P_{pS}$  probabilities would select relatively small but very robust samples of bulge+disk decompositions. Full catalogs of structural parameters are in-

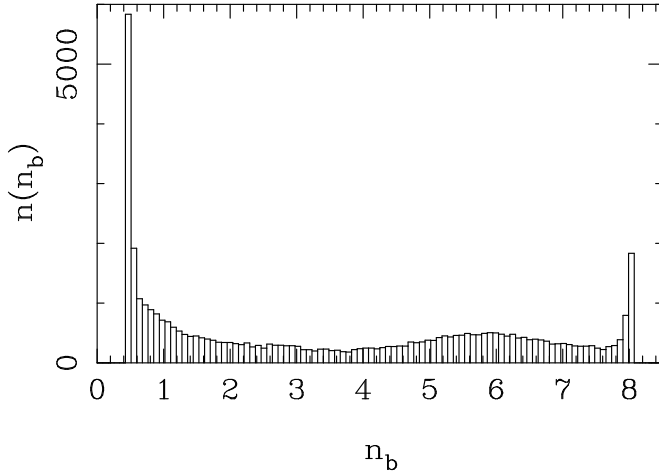


**Figure 15.** Distribution of GIM2D bulge Sérsic index  $n_b$  from the free  $n_b$  bulge + disk decompositions for galaxies with  $(B/T)_{fn} > 0$  and  $P_{pS} \leq 0.32$  and  $P_{n4} \leq 0.32$ . This distribution includes 52,897 galaxies.

cluded here with important cautionary notes on how to select bulge and/or disk subsamples, how to select different morphological types, the issue of bars and the issue of internal dust. These catalogs should provide an extensive comparison set for a wide range of observational and theoretical studies of galaxies.

LS, SLE and DRP gratefully acknowledge financial support from Discovery Grants through the Natural Science and Engineering Research Council of Canada. This research made use of a University of Victoria computing facility funded by grants from the Canadian Foundation for Innovation and the British Columbia Knowledge and Development Fund. We thank the system administrators of this facility for their flawless support. Funding for the creation and distribution of the SDSS Archive has been provided by the Alfred P. Sloan Foundation, the Participating Institutions, the National Aeronautics and Space Administration, the National Science Foundation, the U.S. Department of Energy, the Japanese Monbukagakusho, and the Max Planck Society. The SDSS Web site is <http://www.sdss.org/>. The SDSS is managed by the Astrophysical Research Consortium (ARC) for the Participating Institutions. The Participating Institutions are The University of Chicago, Fermilab, the Institute for Advanced Study, the Japan Participation Group, The Johns Hopkins University, the Korean Scientist Group, Los Alamos National Laboratory, the Max-Planck-Institute for Astronomy (MPIA), the Max-Planck-Institute for Astrophysics (MPA), New Mexico State University, University of Pittsburgh, University of Portsmouth, Princeton University, the United States Naval Observatory, and the University of Washington.

#### REFERENCES

- Abazajian, K. et al. 2009, *ApJS*, 182, 543  
 Allen, P. D. et al. 2006, *MNRAS*, 371, 2  
 Alonso, M. S., Tissera, P. B., Coldwell, G., & Lambas, D. G. 2004, *MNRAS*, 352, 1081  
 Andredakis, Y. C., Peletier, R. F., & Balcells, M. 1995, *MNRAS*, 275, 874  
 Athanassoula, E. 2003, *MNRAS*, 341, 1179  
 Balcells, M. et al. 2003, *ApJ*, 582, 79  
 Benson, A. J., Dzanović, D., Frenk, C. S., & Sharples, R. 2007, *MNRAS*, 379, 841  
 Bertin, E. & Arnouts, S. 1996, *A&AS*, 117, 393  
 Blakeslee, J. P. et al. 2006, *ApJ*, 644, 30  
 Blanton, M. R., & Roweis, S. 2007, *AJ*, 133, 734  
 Blanton, M. R. et al. 2005a, *AJ*, 129, 2562  
 Blanton, M. R. et al. 2005b, *ApJ*, 629, 143  
 Blanton, M. R. et al. 2003, *ApJ*, 592, 819  
 Cheng, J. Y. et al. 2010, *MNRAS*, 412, 727  
 Conselice, C. J. 2006, *MNRAS*, 373, 1389  
 Courteau, S. et al. 2007, *ApJ*, 671, 283  
 Darg, D. W., et al. 2010, *MNRAS*, 401, 1552  
 de Jong, R.S. 1996, *MNRAS*, 313, 45  
 de Souza, R. E., Gadotti, D. A., & dos Anjos, S. 2004, *ApJS*, 153, 411  
 Driver, S. P. et al. 2007, *MNRAS*, 379, 1022  
 Dutton, A. A., & van den Bosch, F. 2009, *MNRAS*, 396, 141  
 Dutton, A. A. et al. 2011a, *MNRAS*, 410, 1660.  
 Dutton, A. A. et al. 2011b, *MNRAS*, in press.  
 Ellison, S. L., Patton, D. R., Simard, L., & McConnachie, Alan W. 2008, *AJ*, 135, 1877  
 Ellison, S. L., Patton, D. R., Simard, L., McConnachie, A. W., Baldry, I. K., & Mendel, J. T. 2010, *MNRAS*, 407, 1514  
 Fall, S., & Efstathiou, G. 1980, *MNRAS*, 193, 189  
 Fisher, D.B., & Drory, N. 2010, *ApJ*, 716, 942  
 Fukugita, M. et al. 2007, *AJ*, 134, 579  
 Governato et al. 2004, *ApJ*, 607, 688  
 Graham, A. W., & Worley, C. C. 2008, *MNRAS*, 388, 1708  
 Hopkins, P. et al. 2010, *ApJ*, 715, 202  
 Im, M. et al. 2002, *ApJ*, 571, 136  
 Kanwar, A., Simard, L., Schade, D., & Gwyn, S. D. J. 2008, *ApJ*, 682, 907  
 Kelly, B. C., & McKay, T. A. 2005, *AJ*, 129, 1287  
 Kormendy, J. 1979, *ApJ*, 227, 714  
 Kormendy, J., & Kennicutt, K. C. 2004, *ARA&A*, 42, 603  
 La Barbera, F. et al. 2010, *MNRAS*, 408, 1313  
 Laurikainen, E. et al. 2010, *MNRAS*, 405, 1089  
 Lintott, C. J. et al. 2008, *MNRAS*, 389, 1179  
 Lotz, J. M., Primack, J., & Madau, P. 2004, *AJ*, 128, 163  
 Lupton, R. et al. 2001, in *ASP Conf. Ser. 238, Astronomical Data Analysis Software and Systems X*, ed. F. R. Harnden, Jr., F. A. Primini, & H. E. Payne (San Francisco: ASP), 269  
 McIntosh, D. H. et al. 2002, *ApJ*, 610, 161  
 Mendel, J. T. et al. 2011, *MNRAS*, in press.  
 Mo, H. J., Mao, S., & White, S. D. M. 1998, *MNRAS*, 295, 319  
 Patton, D. R., Ellison, S. L., Simard, L., McConnachie, A. W., & Mendel, J.T. 2011, *MNRAS*, 412, 591  
 Pignatelli, E., Fasano, G., & Cassata, P. 2006, *A&A*, 446, 373  
 Peng, C. Y. et al. 2002, *AJ*, 124, 266  
 Perez, J., Tissera, P., Padilla, N., Alonso, M. S., & Lambas, D. G. 2009, *MNRAS*, 399, 1157  
 Robertson, B. et al. 2004, *ApJ*, 606, 32  
 Shen, S. et al. 2003, *MNRAS*, 343, 978  
 Simard, L. et al. 2002, *ApJS*, 142, 1  
 Simard, L. et al. 2009, *A&A*, 508, 1141  
 Strauss, M. A. et al. 2002, *ApJ*, 124, 1810  
 Thanjavur, K., & Simard, L. 2011, *ApJ*, submitted.  
 Tran, K.-V. H. et al. 2003, *ApJ*, 590, 238  
 Wijesinghe, D. B. et al. 2010, *MNRAS*, 404, 2077

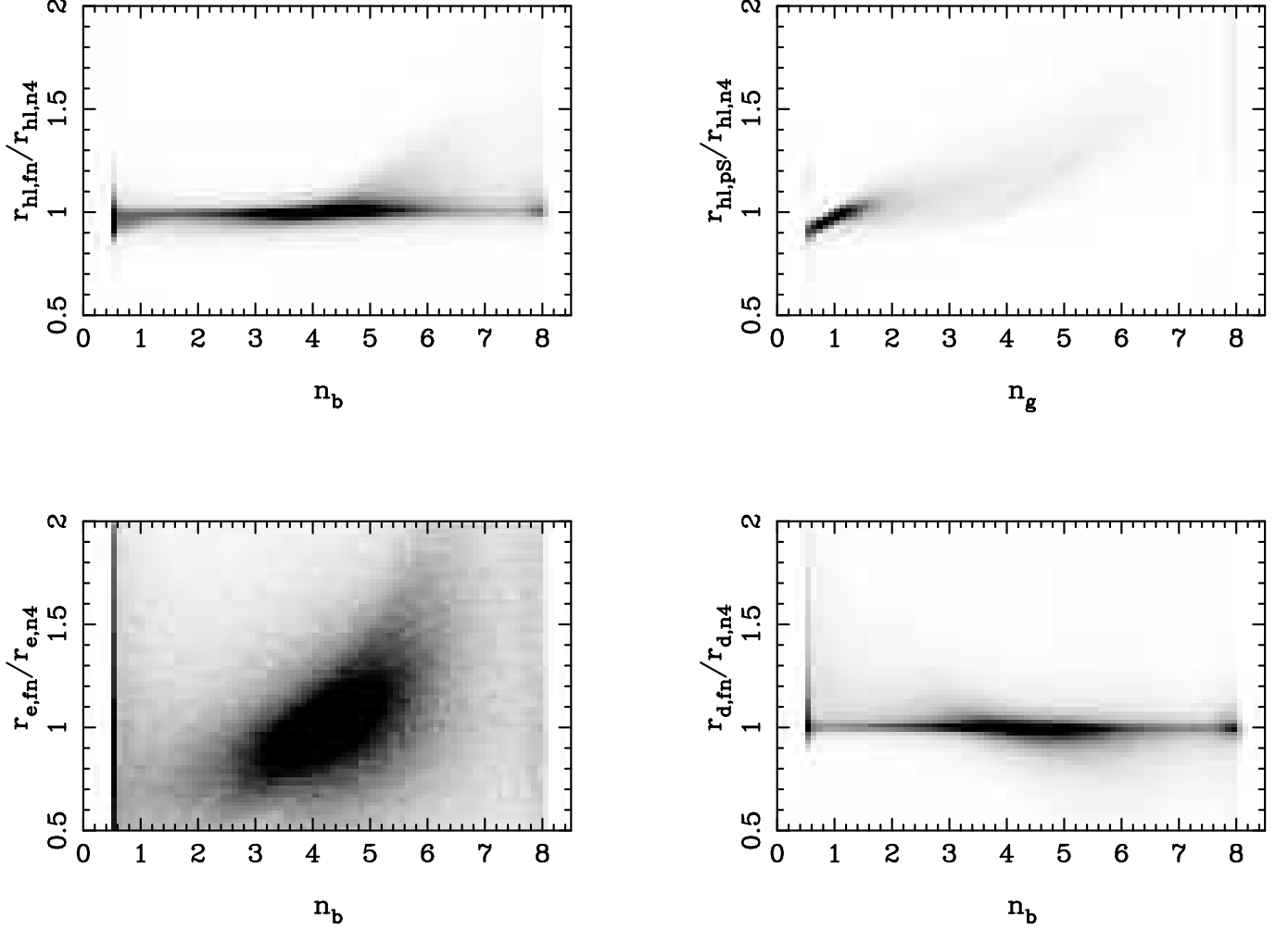


**Figure 16.** Comparison of  $r$ -band GIM2D radii measured from three different fitting models. *Top left:* Ratio of the galaxy half-light radii  $r_{hl,fn}$  and  $r_{hl,n4}$  from the free  $n_b$  bulge + disk and  $n_b = 4$  bulge + disk decompositions versus bulge Sérsic index  $n_b$ . *Top right:* Ratio of the galaxy half-light radii  $r_{hl,pS}$  and  $r_{hl,n4}$  from the single component, pure Sérsic fits and  $n_b = 4$  bulge + disk decompositions versus the galaxy Sérsic index  $n_g$ . *Bottom left:* Ratio of the bulge effective radii  $r_{e,fn}$  and  $r_{e,n4}$  from the free  $n_b$  bulge + disk and  $n_b = 4$  bulge + disk decompositions versus bulge Sérsic index  $n_b$ . *Bottom right:* Ratio of the disk scale lengths  $r_{d,fn}$  and  $r_{d,n4}$  from free  $n_b$  bulge + disk and  $n_b = 4$  bulge + disk decompositions versus bulge Sérsic index  $n_b$ . The greyscale represents the two-dimensional distribution of galaxies normalized by the total number of galaxies. The  $x$ -axis and  $y$ -axis bin sizes for the two-dimensional distributions were 0.1 and 0.02 respectively. The limits for the greyscale go from zero to 50% of the peak value of the normalized distribution.

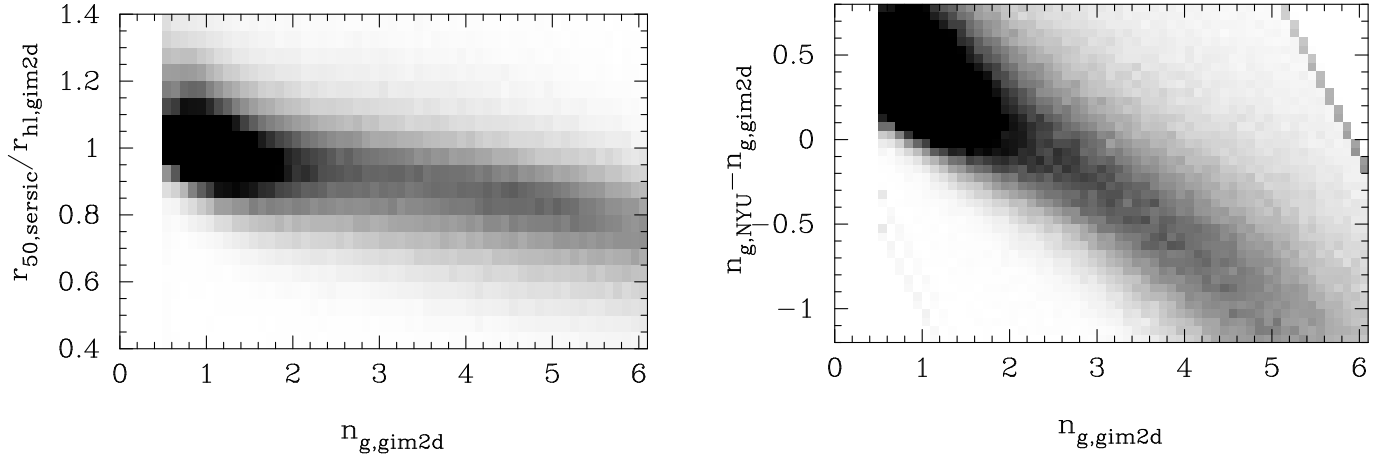


**Figure 17.** Comparison between NYU and GIM2D pure Sérsic structural parameters. *Left:* Ratio of the NYU and circularized GIM2D galaxy half-light radii  $r_{50,seraic}$  and  $r_{hl,gim2d}$  versus the GIM2D galaxy Sérsic index  $n_{g,gim2d}$ . *Right:* Difference between the NYU and GIM2D galaxy Sérsic indices versus GIM2D galaxy Sérsic index  $n_{g,gim2d}$ . The greyscale represents the two-dimensional distribution of galaxies normalized by the total number of galaxies. The  $x$ -axis and  $y$ -axis bin sizes for the two-dimensional distributions were 0.1 and 0.05 respectively. The limits for the greyscale go from zero to 30% of the peak value of the normalized distribution.

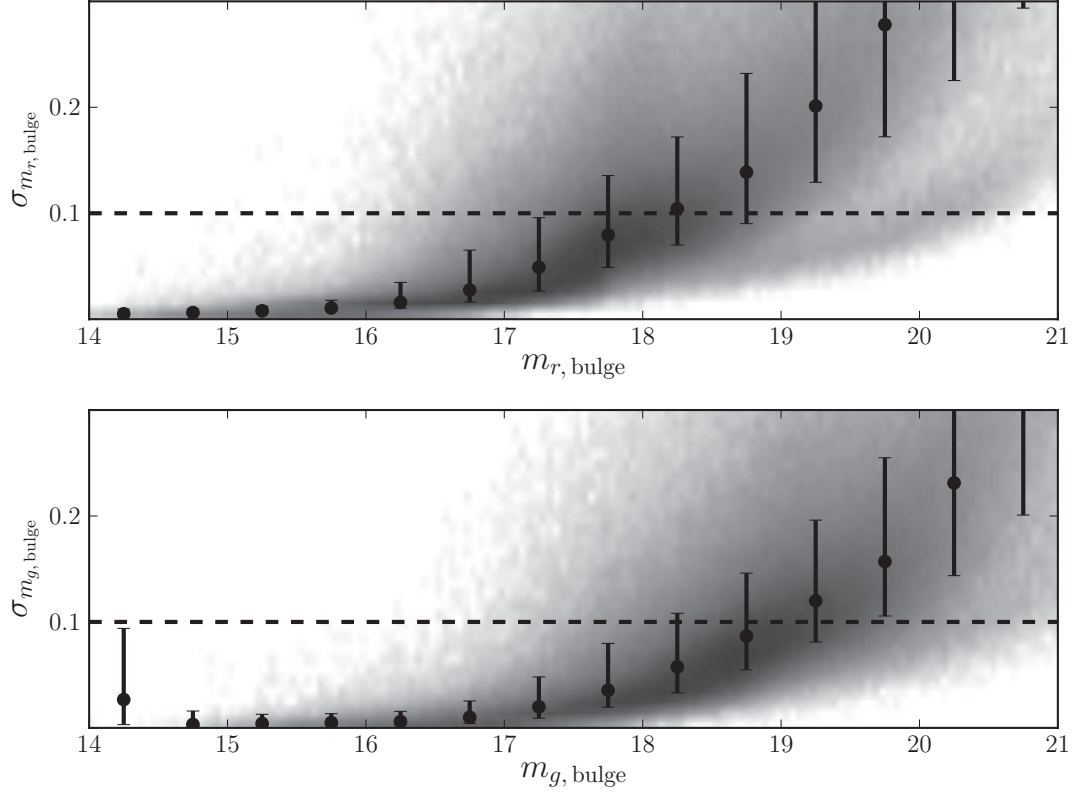


**Figure 18.** GIM2D bulge  $g$  and  $r$  photometric errors as a function of bulge magnitude in  $n=4$  bulge+disk decompositions. Bulge magnitudes were calculated using Equations 3c and 3d. Errors on total galaxy magnitudes and bulge fractions were propagated through these equations to obtain the photometric errors. The data points are median values, and the error bars are the 16th and 84th percentile values.

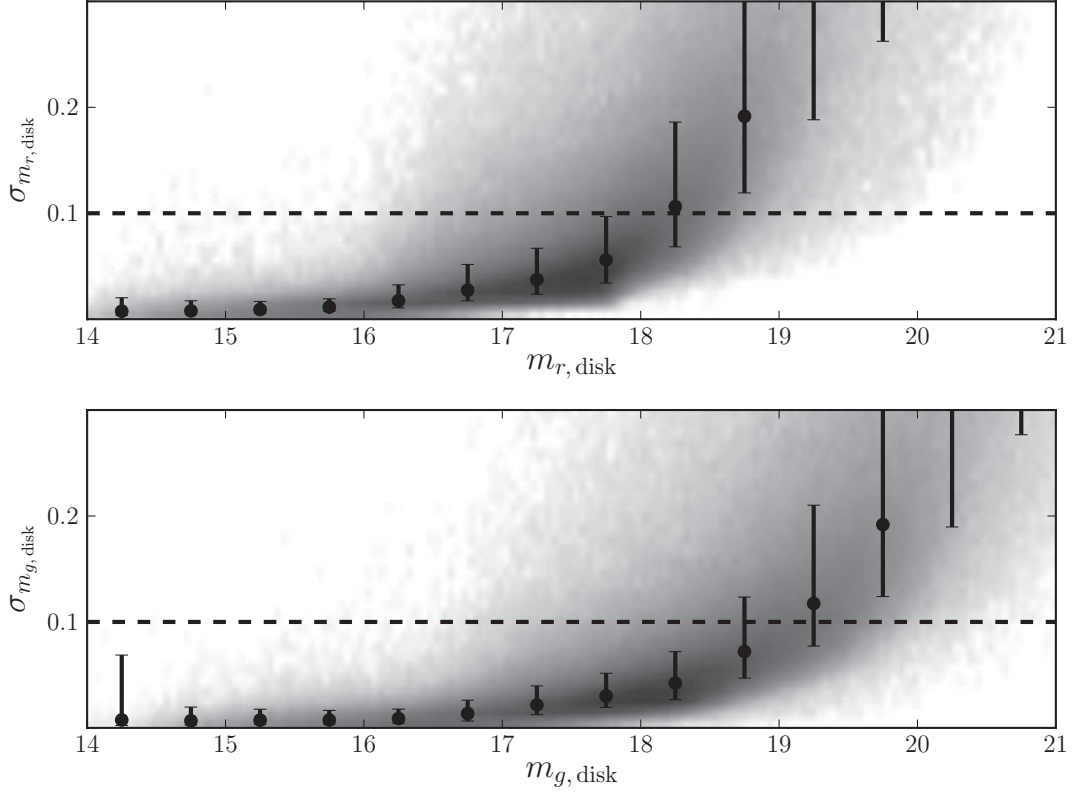


**Figure 19.** GIM2D disk  $g$  and  $r$  photometric errors as a function of disk magnitude in  $n=4$  bulge + disk. Disk magnitudes were calculated using Equations 3e and 3f. Errors on total galaxy magnitudes and bulge fractions were propagated through these equations to obtain the photometric errors. The data points are median values, and the error bars are the 16th and 84th percentile values.

**Table 1**  
SDSS structural parameters from  $n_b=4$  bulge + disk decompositions (Table available in online electronic version)

Column Name	Description
ObjID	SDSS Object ID
$z$	SDSS Redshift (Spectroscopic if available. Photometric otherwise)
SpecClass	SDSS SpecClass value (set to $-1$ if $z$ is photometric or $-2$ if no redshift available at all)
Scale	Physical scale in arcsec/kpc at redshift $z$
$V_{max}$	Galaxy volume correction in $\text{Mpc}^3$ (Equation 7)
$g_{g2d}$	$g$ -band apparent magnitude of GIM2D output B+D model (Equation 1)
$r_{g2d}$	$r$ -band apparent magnitude of GIM2D output B+D model (Equation 1)
$g_{g2d,f}$	$g$ -band apparent fiber magnitude of output B+D model
$r_{g2d,f}$	$r$ -band apparent fiber magnitude of output B+D model
$\Delta(\text{fiber color})$	Delta fiber color defined as $(g-r)_{gim2d,fiber} - (g-r)_{SDSS,fiber}$ (set to $-99.99$ if no SDSS fiber magnitudes available)
$(B/T)_g$	$g$ -band bulge fraction
$(B/T)_r$	$r$ -band bulge fraction
$(B/T)_{g,f}$	$g$ -band fiber bulge fraction
$(B/T)_{r,f}$	$r$ -band fiber bulge fraction
$R_{hl,g}$	$g$ -band galaxy semi-major axis, half-light radius in kiloparsecs
$R_{hl,r}$	$r$ -band galaxy semi-major axis, half-light radius in kiloparsecs
$R_{chl,g}$	$g$ -band galaxy circular half-light radius in kiloparsecs
$R_{chl,r}$	$r$ -band galaxy circular half-light radius in kiloparsecs
$R_e$	Bulge semi-major effective radius in kiloparsecs (Equation 2)
$e$	Bulge ellipticity ( $e \equiv 1 - b/a$ , $e = 0$ for a circular bulge)
$\phi_b$	Bulge position angle in degrees (measured clockwise from the $+y$ axis of SDSS images)
$R_d$	Exponential disk scale length in kiloparsecs (Equation 2)
$i$	Disk inclination angle in degrees ( $i \equiv 0$ for a face-on disk)
$\phi_d$	Disk position angle in degrees (measured clockwise from the $+y$ axis of SDSS images)
$(dx)_g$	B+D model center offset from column position given by <code>colc_g</code> on SDSS corrected $g$ -band image (arcsec)
$(dy)_g$	B+D model center offset from row position given by <code>rowc_g</code> on SDSS corrected $g$ -band image (arcsec)
$(dx)_r$	B+D model center offset from column position given by <code>colc_r</code> on SDSS corrected $r$ -band image (arcsec)
$(dy)_r$	B+D model center offset from row position given by <code>rowc_r</code> on SDSS corrected $r$ -band image (arcsec)
$S2_g$	$g$ -band image smoothness parameter (as defined in Simard et al. (2009))
$S2_r$	$r$ -band image smoothness parameter (as defined in Simard et al. (2009))
$M_{g,g}$	$g$ -band GIM2D galaxy rest-frame, absolute magnitude (Equation 3a)
$M_{g,b}$	$g$ -band GIM2D bulge rest-frame, absolute magnitude (Equation 3c)
$M_{g,d}$	$g$ -band GIM2D disk rest-frame, absolute magnitude (Equation 3e)
$M_{r,g}$	$r$ -band GIM2D galaxy rest-frame, absolute magnitude (Equation 3b)
$M_{r,b}$	$r$ -band GIM2D bulge rest-frame, absolute magnitude (Equation 3d)
$M_{r,d}$	$r$ -band GIM2D disk rest-frame, absolute magnitude (Equation 3f)
$n_b$	Bulge Sérsic index
$P_{pS}$	$F$ -test probability that a B+D model is <i>not</i> required compared to a pure Sérsic model

**Table 2**SDSS structural parameters from free  $n_b$  bulge + disk decompositions (Table available in online electronic version)

Column Name	Description
ObjID	SDSS Object ID
$z$	SDSS Redshift (Spectroscopic if available. Photometric otherwise)
SpecClass	SDSS SpecClass value (set to $-1$ if $z$ is photometric or $-2$ if no redshift available at all)
Scale	Physical scale in arcsec/kpc at redshift $z$
$V_{max}$	Galaxy volume correction in $\text{Mpc}^3$ (Equation 7)
$g_{g2d}$	$g$ -band apparent magnitude of GIM2D output B+D model (Equation 1)
$r_{g2d}$	$r$ -band apparent magnitude of GIM2D output B+D model (Equation 1)
$g_{g2d,f}$	$g$ -band apparent fiber magnitude of output B+D model
$r_{g2d,f}$	$r$ -band apparent fiber magnitude of output B+D model
$\Delta(\text{fiber color})$	Delta fiber color defined as $(g - r)_{gim2d,fiber} - (g - r)_{SDSS,fiber}$ (set to $-99.99$ if no SDSS fiber magnitudes available)
$(B/T)_g$	$g$ -band bulge fraction
$(B/T)_r$	$r$ -band bulge fraction
$(B/T)_{g,f}$	$g$ -band fiber bulge fraction
$(B/T)_{r,f}$	$r$ -band fiber bulge fraction
$R_{hl,g}$	$g$ -band galaxy semi-major axis, half-light radius in kiloparsecs
$R_{hl,r}$	$r$ -band galaxy semi-major axis, half-light radius in kiloparsecs
$R_{chl,g}$	$g$ -band galaxy circular half-light radius in kiloparsecs
$R_{chl,r}$	$r$ -band galaxy circular half-light radius in kiloparsecs
$R_e$	Bulge semi-major effective radius in kiloparsecs (Equation 2)
$e$	Bulge ellipticity ( $e \equiv 1 - b/a$ , $e = 0$ for a circular bulge)
$\phi_b$	Bulge position angle in degrees (measured clockwise from the $+y$ axis of SDSS images)
$R_d$	Exponential disk scale length in kiloparsecs (Equation 2)
$i$	Disk inclination angle in degrees ( $i \equiv 0$ for a face-on disk)
$\phi_d$	Disk position angle in degrees (measured clockwise from the $+y$ axis of SDSS images)
$(dx)_g$	B+D model center offset from column position given by <code>colc_g</code> on SDSS corrected $g$ -band image (arcsec)
$(dy)_g$	B+D model center offset from row position given by <code>rowc_g</code> on SDSS corrected $g$ -band image (arcsec)
$(dx)_r$	B+D model center offset from column position given by <code>colc_r</code> on SDSS corrected $r$ -band image (arcsec)
$(dy)_r$	B+D model center offset from row position given by <code>rowc_r</code> on SDSS corrected $r$ -band image (arcsec)
$S2_g$	$g$ -band image smoothness parameter (as defined in Simard et al. (2009))
$S2_r$	$r$ -band image smoothness parameter (as defined in Simard et al. (2009))
$M_{g,g}$	$g$ -band GIM2D galaxy rest-frame, absolute magnitude (Equation 3a)
$M_{g,b}$	$g$ -band GIM2D bulge rest-frame, absolute magnitude (Equation 3c)
$M_{g,d}$	$g$ -band GIM2D disk rest-frame, absolute magnitude (Equation 3e)
$M_{r,g}$	$r$ -band GIM2D galaxy rest-frame, absolute magnitude (Equation 3b)
$M_{r,b}$	$r$ -band GIM2D bulge rest-frame, absolute magnitude (Equation 3d)
$M_{r,d}$	$r$ -band GIM2D disk rest-frame, absolute magnitude (Equation 3f)
$n_b$	Bulge Sérsic index
$P_{pS}$	$F$ -test probability that a B+D model is <i>not</i> required compared to a pure Sérsic model
$P_{n4}$	$F$ -test probability that a free $n_b$ B+D model is <i>not</i> required compared to a fixed $n_b=4$ B+D model



**Table 3**  
SDSS structural parameters from pure Sérsic decompositions (Table available in online electronic version)

Column Name	Description
ObjID	SDSS Object ID
$z$	SDSS Redshift (Spectroscopic if available. Photometric otherwise)
SpecClass	SDSS SpecClass value (set to $-1$ if $z$ is photometric or $-2$ if no redshift available at all)
Scale	Physical scale in arcsec/kpc at redshift $z$
$V_{max}$	Galaxy volume correction in $\text{Mpc}^3$ (Equation 7)
$g_{g2d}$	$g$ -band apparent magnitude of GIM2D output pure Sérsic model (Equation 1)
$r_{g2d}$	$r$ -band apparent magnitude of GIM2D output pure Sérsic model (Equation 1)
$g_{g2d,f}$	$g$ -band apparent fiber magnitude of output pure Sérsic model
$r_{g2d,f}$	$r$ -band apparent fiber magnitude of output pure Sérsic model
$\Delta(\text{fiber color})$	Delta fiber color defined as $(g - r)_{gim2d,fiber} - (g - r)_{SDSS,fiber}$ (set to $-99.99$ if no SDSS fiber magnitudes available)
$R_{hl,g}$	$g$ -band galaxy semi-major axis, half-light radius in kiloparsecs
$R_{hl,r}$	$r$ -band galaxy semi-major axis, half-light radius in kiloparsecs
$R_{chl,g}$	$g$ -band galaxy circular half-light radius in kiloparsecs
$R_{chl,r}$	$r$ -band galaxy circular half-light radius in kiloparsecs
$e$	Galaxy ellipticity ( $e \equiv 1 - b/a$ , $e = 0$ for a circular galaxy)
$\phi_b$	Galaxy position angle in degrees (measured clockwise from the $+y$ axis of SDSS images)
$(dx)_g$	Pure Sérsic model center offset from column position given by <code>colc_g</code> on SDSS corrected $g$ -band image (arcsec)
$(dy)_g$	Pure Sérsic model center offset from row position given by <code>rowc_g</code> on SDSS corrected $g$ -band image (arcsec)
$(dx)_r$	Pure Sérsic model center offset from column position given by <code>colc_r</code> on SDSS corrected $r$ -band image (arcsec)
$(dy)_r$	Pure Sérsic model center offset from row position given by <code>rowc_r</code> on SDSS corrected $r$ -band image (arcsec)
$S2_g$	$g$ -band image smoothness parameter (as defined in Simard et al. (2009))
$S2_r$	$r$ -band image smoothness parameter (as defined in Simard et al. (2009))
$M_{g,g}$	$g$ -band GIM2D galaxy rest-frame, absolute magnitude (Equation 3a)
$M_{r,g}$	$r$ -band GIM2D galaxy rest-frame, absolute magnitude (Equation 3b)
$n_g$	Galaxy Sérsic index